SHIBAURA INSTITUTE OF TECHNOLOGY

Non-linear Analysis of Electrical and Thermal Stress Grading System in Multi-Level Inverter-Driven Medium Voltage Motors

by

Nguyen Nhat Nam

A thesis submitted to Shibaura Institute of Technology

in fulfilment of the requirements for the degree of

Doctor Engineering

Graduate School of Engineering and Science

September 2014

Declaration of Authorship

I, **Nguyen Nhat Nam**, declare that this thesis titled, **Non-linear Analysis of Electrical and Thermal Stress Grading System in Multi-Level Inverter-Driven Medium Voltage Motors**, and the work presented in it are my own. I confirm that:

- This work was done wholly while in candidature for a research degree at Shibaura Institute of Technology.
- Where I have consulted the works of others, this is always clearly declared.
- The sources of quotations from the works of others are always given.
- With the exception of quotations, and the model of Series Connected H-Bridge Voltage Source Converter, this thesis is entirely my own work.

Signed: _____

(NGUYEN NHAT NAM)

Certified by: S. Matsumoto

(PROFESSOR SATOSHI MATSUMOTO)

Date: September 08th, 2014

SHIBAURA INSTITUTE OF TECHNOLOGY

ABSTRACT

Advanced Research Program on Environmental Energy Engineering

Graduate School of Engineering and Science

by Nguyen Nhat Nam

Energy has been one of the most important problems in the world. Beside numerous efforts to explore and to apply renewable resources of energy, the efficient use of energy has become a good solution to face the depleted situation of fossil fuels. In practice, applications of adjustable speed drives are demonstrated being able to enhance the efficiency of using electric power. However, this trend becomes a big challenge for stress grading systems of stator end-winding insulations in AC motors because of fast and high voltage impulses in the output of the frequency-variable drives. Hence, a comprehensive understanding about the behaviour of stress grading systems in the inverter source conditions is an inevitable demand. Originated from this desire, the aim of our research work is to analyze the electrical and the thermal stress grading mechanisms of a typical stress grading system in invert-fed medium voltage motors.

Based on a finite element method software package named COMSOL, two models of electric field and heat transfer analyses are developed taking into account the nonlinearly electrical behaviour of the semiconductive tape in the stress grading systems. Besides, a mathematical model of surge travelling is

modified and built in Matlab/Simulink to compute overshot voltages at the motor terminal caused by the cable-motor impedance mismatch.

In the inverter applied conditions, the electric field stress and the dissipated power in the conductive armour tape of the stress grading system are validated existing during the short rise time interval of the impulses. The dissipated power density is observed to be greatest in the area at the stator slot exits, hence the highest temperature rise locates in this region. Moreover, the effects of voltage overshooting and ringing due to the cable-motor impedance mismatch on the stress grading system behaviour are clarified in detail. This phenomenon can increase both the intensity and the lasting time of the electric and thermal stresses, exacerbate the ineffective situation of the stress grading system, especially in the cases of long connecting cables, high cable-motor surge impedance differences, and newer inverters with very fast electronic switches.

With the results achieved above, the application of our simulation models can be a promising way for the improvements and optimal designs of stress grading system compatible to inverter-fed motors.

Acknowledgements

I would like to express my highest gratitude to Professor Satoshi Matsumoto for his enthusiastic guidance, valuable suggestions and helps not only in the research work but also in my daily life.

Financial supports from Japan International Cooperation Agency (JICA) for my study and living are highly appreciated.

I gratefully acknowledge my examination committee members; Professor Hiroyuki Nishikawa, Professor Goro Fujita, Professor Kan Akatsu, and Professor Akiko Kumada for their valuable comments and kindly cooperation in reviewing my research work.

I would like to thank Emeritus Professor Yoshikazu Shibuya for his useful advices and encouragements during my research work.

I am thankful to my dear friend, Mr. Le Dinh Khoa for allowing me to use his simulation model of Series Connected H-Bridge Voltage Source Converter, and for all his useful discussions. Special acknowledgement is sent to Mr. Takahiro Nakamura from Tokyo University for his precious experiment information.

The helps and supports from Ms. Junko Okura, Ms. Makiko Hagiwara and Mr. Seiji Mizuno of JICA during my living in Japan are highly appreciated.

I would like to thank all the members of Matsumoto Laboratory, and University staffs at Shibaura Institute of Technology, especially the Global Initiative Section and Graduate School Section for all their helps and supports.

Finally, I would like to acknowledge the endless supports from my family including my grandparents, my parents, my beloved wife, my sister and my brother in law.

I would like to devote this thesis to my grandfather…

CONTENTS

Declaration of Authorship i

Abstract ii

Acknowledgements iv

List of Figures viii

List of Tables xiii

Abbreviations xiv

Symbols xv

1 Introduction 1

1.1 Preface *1*

1.2 Stress grading system structure *2*

1.2.1 Conductive armour tape *2*

1.2.2 Semiconductive tape *4*

1.3 Temperature and field dependence of materials in stress grading systems *5*

1.4 Literature review *9*

1.5 Objective of the present study *16*

1.6 Thesis outline *17*

2 Modelling 19

2.1 Approaches applied for stress grading analysis in previous works *19*

2.2 FEM based models of stress grading system *22*

2.2.1 Electric field analysis model 22

2.2.2 Heat transfer analysis model 26

2.3 Series Connected H-Bridge voltage source converter model... 31

2.4 Mathematical model for PWM surge transmission in ASD networks 32

3 Results 36

3.1 Frequency response of the stress grading system..... 36

3.2 Operation analysis of the stress grading system under PWM voltage sources..... 40

3.2.1 Output voltages of the SCHB VSCs..... 40

3.2.2 Electric field analysis..... 43

3.2.3 Heat transfer analysis 48

3.3 Investigation of the effect of overshot voltage due to impedance mismatch between cable and motor 50

3.3.1 Fundamental case 50

3.3.2 Typical cases 55

4 Discussion 60

4.1 Electric field and thermal stresses in the SGS..... 60

4.2 Validation of the FEM based analysis models..... 65

5 Conclusion and Future works 70

5.1 Conclusion 70

5.2 Future works 71

A List of publication 74

References 77

List of Figures

Fig. 1-1: *A general configuration of inverter-driven motor* 2

Fig. 1-2: *A typical structure of type II form wound insulation system* 3

Fig. 1-3: *Microstructure view of semiconductive materials based on SiC and ZnO* [8] 4

Fig. 1-4: *Measuring samples of CAT or SCT in* [111] 7

Fig. 1-5: *DC resistivity of CAT measured at 22* °C, *80* °C, *110* °C *and 155* °C *in* [11] 7

Fig. 1-6: *DC resistivity of SCT measured at 22* °C, *80* °C, *110* °C *and 155* °C *in* [11]. 8

Fig. 1-7: *Electric field dependent curves of the electrical conductivity of SCT measured at DC, 60* Hz, *3* kHz *and 5* kHz *in* [12] 8

Fig. 1-8: *A typical stress grading configuration for optimization problem in* [13] 9

Fig. 1-9: *Spark gap generator circuit proposed in* [18] 12

Fig. 1-10: *Sectionalized structure of stress grading system with an additional conductive tape in* [19]. 13

Fig. 1-11: *Illustration of capacitive stress grading systems using embedded foils.* 15

Fig. 2-1: *Equivalent circuit of a stress grading system* [26,30-31]. 20

Fig. 2-2: *Schwarz-Christoffel conformal transformation mapping plane* (z) *onto plane* (ζ) [13, 32] 20

Fig. 2-3: *Detailed size of the studied stress grading system in 2D axially symmetric coordinate (r, z).* 24

Fig. 2-4: *Electrical conductivity of the materials versus electric field strength.* 25

Fig. 2-5: *Boundary conditions used in the electric field analysis models.* 25

Fig. 2-6: *A typical cooling system for high power motors* [37]. 28

Fig. 2-7: *Boundary conditions used in the heat transfer analysis model.* 28

Fig. 2-8: *The mesh profile of the SGS used in the two analysis models.* 30

Fig. 2-9: *Typical topology of a (2M+1)-level SCHB VSC* [1, 42]. 32

Fig. 2-10: *Computation algorithm of V_M for Matlab/Simulink used in* [45] 35

Fig. 2-11: *Improved computation algorithm of V_M for Matlab/Simulink in this work.* 35

Fig. 3-1: *Electric potential and tangential electric field stress on the surfaces of the SGS in case of 50 Hz sinusoidal voltage source.* 36

Fig. 3-2: *Maximum value along z-axis of average dissipated power density in the SGS and maximum temperature on the surfaces of the SGS in case of 50 Hz sinusoidal voltage source.* 37

Fig. 3-3: *Maximum tangential electric field stress on the surfaces of the CAT and the SCT in case of sinusoidal voltage sources with the frequency from 50 Hz to 5 MHz.* 38

Fig. 3-4: *Maximum tangential electric field stress on the surfaces of the SGS in the four cases 50 Hz, 26 kHz, 123 kHz and 5 MHz sinusoidal voltages.* 39

Fig. 3-5: *Maximum temperature on the surfaces of the CAT and the SCT in case of sinusoidal voltage sources with the frequency from 50 Hz to 20 kHz.* *39*

Fig. 3-6: *Electric potential and tangential electric field stress on the surfaces of the SGS in case of 5 MHz sinusoidal voltage source.* *40*

Fig. 3-7: *Output phase-to-ground voltages of the 5L SCHB and 11L SCHB VSCs.* *41*

Fig. 3-8: *Harmonic spectra in the phase-to-ground voltages of the 5L and the11L SCHB VSCs.* *42*

Fig. 3-9: *Maximum tangential electric field stress on the surfaces of the SGS in the three cases of 5L, 11L SCHB VSCs and 9 kV_{RMS} (phase-to-phase) sinusoidal voltage source.* *43*

Fig. 3-10: *Tangential electric field on the surfaces of the SGS at the two points (z = 0 mm and z = 56.9 mm) in the two cases of 5L and 11L SCHB VSCs during the interval from 10 ms to 20 ms* *44*

Fig. 3-11: *Tangential electric field on the surfaces of the SGS at the two points (z = 0 mm and z = 56.9 mm) in the case of 5L SCHB VSC during the interval from 12.14 ms to 12.18 ms.* *45*

Fig. 3-12: *Tangential electric field on the surfaces of the SGS at the two points (z = 0 mm and z = 56.9 mm) in the case of 11L SCHB VSC during the interval from 12.445 ms to 12.475 ms.* *45*

Fig. 3-13: *Distribution of electric potential and tangential electric field on the surfaces of the SGS during the interval from 12.14 ms to12.18 ms in the case of 5L SCHB VSC..* *47*

Fig. 3-14: *Distribution of electric potential and tangential electric field on the surfaces of the SGS during the interval from 12.445 ms to12.475 ms in the case of 11L SCHB VSC.. ..... 47*

Fig. 3-15: *Maximum value along z-axis of average dissipated power density in the SGS in the cases of 5L and 11L SCHB VSCs. 48*

Fig. 3-16: *Temperature distribution on the surfaces of the SGS in the three cases of 11L, 5L SCHB VSCs and sinusoidal voltage source after 30 hours. 49*

Fig. 3-17: *Comparison of maximum tangential electric field stress on the surfaces of the SGS under the 11L SCHB voltages between the two cases without and with voltage overshooting. 51*

Fig. 3-18: *Tangential electric field on the surfaces of the SGS at the two points (z = 0 mm and z =56.9 mm) in the cases of 11L SCHB voltages during the interval from 10.72 ms to 10.75 ms. 52*

Fig. 3-19: *Tangential electric field on the surfaces of the SGS at the two points (z = 0 mm and z = 56.9 mm) in the cases of 11L SCHB voltages during the interval from 12.445 ms to 12.475 ms 53*

Fig. 3-20: *Maximum value along z-axis of average dissipated power density in the SGS in the cases of 11L SCHB voltages without and with voltage overshooting.. ..... 54*

Fig. 3-21: *Temperature distribution on the surfaces of the SGS in the cases of 11L SCHB voltages without and with voltage overshooting after 30 hours..... 54*

Fig. 3-22: *Simplified waveform of the 11L SCHB VSC used in the ns-scaled electric field analysis.* *56*

Fig. 3-23: *Tangential electric field stress at z = 0 mm on the surface of the CAT under the simplified and the 11L SCHB voltages.* *57*

Fig. 3-24: *Voltage overshot factor versus the cable length for the two motor impedance values of 100 Ω and 1000 Ω.* *58*

Fig. 3-25: *Maximum tangential electric field on the CAT at z =0 versus the rise time of the inverter voltages.* *59*

Fig. 4-1: RC *low pass filter circuit.* *60*

Fig. 4-2*: Frequency response of a low pass filter output* *61*

Fig. 4-3*: Maximum values along z-axis of dissipated power density in the SGS* *66*

Fig. 4-4: *Computation results* *67*

Fig. 4-5*: Hypothesis explained for PD on the middle surface of CAT in* [29] . *69*

List of Tables

Table 2-1: *Electrical properties of the materials* ..... .24

Table 2-2: *Thermal properties of the materials* 26

Table 2-3: *Basic data of the SCHB VSCs.* 31

Table 3-1: *Fundamental harmonic and THD of the phase voltage provided by the 5L and the 11L SCHB VSCs.* 42

Table 3-2: *Amplitude, appearance time and location of maximum tangential electric field stress on the surface of the SGS in the three cases of 5L, 11L SCHB VSCs and 9 kV_{RMS} (phase-to-phase) sinusoidal voltage source.* 44

Table 3-3: *Important differences of tangential electric field stress at the two special positions on the SGS in the cases of 5L and the 11L SCHB VSCs.* 46

Table 3-4: *Important data of temperature distribution in the SGS from the heat transfer analyses.* 49

Table 3-5: *Surge characteristics of the inverter, the cable and the motor in the fundamental case.* 50

Table 4-1: *Voltage ratios of the CAT and the SCT.* 62

Table 4-2: *Comparison between our computation and the experiment in [50].* 68

Abbreviations

11L	11-Level
2D	Two Dimensional
3D	Three Dimensional
5L	5-Level
AC	Alternating Current
ASD	Adjustable Speed Drive
CAT	Conductive Armour Tape
DC	Direct Current
EMTDC	Electromagnetic Transient and DC
EMTP	Electromagnetic Transient Program
FC VSC	Flying Capacitor Voltage Source Converter
FEM	Finite Element Method
FH	Fundamental Harmonic
ICCD	Intensified Charge-Couple Device
NPC VSC	Neutral Point Clamed Voltage Source Converter
PD	Partial Discharge
PSCAD	Power Systems Computer Aided Design
PWM	Pulse Width Modulation
RMS	Root Mean Square
SCHB VSC	Series Connected H-Bridge Voltage Source Converter
SCT	Semiconductive Tape
SGS	Stress Grading System
SiC	Silicon Carbide
THD	Total Harmonic Distortion
TS	Technical Specification
VPI	Vacuum Pressure Impregnation
ZnO	Zinc Oxide

Symbols

$\|E_{tan}\|_{max}$	Maximum tangential electric field stress	(V/m)
E_{tan}	Tangential electric field stress	(V/m)
$\vec{B}$	Magnetic flux density vector	(Wb/m^2)
C_C	Cable capacitance per unit length	(F/m)
C_{INS}	Capacitance of main insulation in SGS	(F)
C_M	Motor capacitance	(F)
C_p	Heat capacity	($JKg^{-1}K^{-1}$)
$\vec{D}$	Electric flux density vector	(C/m^2)
ΔT	Temperature rise	(^oC)
ΔT_{max}	Maximum temperature rise limitation	(^oC)
$\Delta \tau$	Chosen duration of time	(s)
ε	Electrical permittivity	(F/m)
E	Absolute value of the electric field intensity vector	(V/m)
$\vec{E}$	Electric field intensity vector	(V/m)
ε_i	Electrical permittivity of the insulation	(F/m)
ε_v	Electrical permittivity of the varnish	(F/m)
ε_{ra}	Emissivity coefficient	(pu)
E_{tan}	Tangential electric field stress	(V/m)
F	Electric flux	(Vm)
f_{ca}	Frequency of triangular carrier wave	(Hz)
f_c	Cut-off frequency of low pass filter	(Hz)
f_e	Equivalent frequency of a voltage rise time	(Hz)
f_{eff}	Effective frequency of multi-level inverter	(Hz)
$\vec{H}$	Magnetic field intensity vector	(A/m)
h	Heat transfer coefficient	($Wm^{-2}K^{-1}$)
$\vec{J}$	Electric current density vector	(A/m^2)
k	Thermal conductivity	($Wm^{-1}K^{-1}$)
K_M	Reflection constant at the cable-motor interface	(pu)
K_S	Reflection constant at the cable-inverter interface	(pu)
l	Length of Cable, CAT, SCT	(m)
L_C	Cable inductance per unit length	(H/m)
l_c	Cable critical length	(m)
l_{eff}	Effectively working length of SCT	(m)

L_M	Motor inductance	(H)
M	Number of H-Bridge cells	(pu)
$\vec{n}$	Unit normal vector	(pu)
Q	Heat source density	(W/m^3)
$\bar{Q}_{res}$	Average dissipated power density	(W/m^3)
Q_{res}	Dissipated power density	(W/m^3)
r	Radial position in the cylindrical coordinate system	(m)
r_c	Radius of conductor in SGS	(m)
R_{SCT}	Resistance of SCT	(Ω)
ρ	Mass density	(Kg/m^3)
ρ_{ec}	Volumetric resistivity	(Ωm)
ρ_s	Surface resistivity	(Ω)
σ_{ec}	Electrical conductivity	(S/m)
$\bar{\sigma}_{ec}$	Average electrical conductivity	(S/m)
σ_i	Electrical conductivity of the insulation	(S/m)
σ_v	Electrical conductivity of the varnish	(S/m)
T	Temperature	(K) or (^oC)
T_{max}	Critical temperature	(^oC)
τ	Travelling time of surge	(s)
t	Time	(s)
t_0	Chosen point of time	(s)
T_{ext}	External temperature	(K) or (^oC)
t_{ins}	Thickness of main insulation in SGS	(m
t_r	Rise time of impulse voltage	(s)
$\vec{u}$	Velocity vector	(m/s)
$u_S(t)$	Unit step function	(pu)
U_J	Jump voltage	(V)
U_P	Peak voltage	(V)
V	Electric potential	(V)
v	Travelling velocity of surge	(m/s)
V_{CAT}	Electric difference on CAT	(V)
V_D	Electric difference on a SCT segment	(V)
V_M	Voltage at the motor side	(V)
V_O	Output voltage of a low pass filter	(V)
Vs	Applied voltage or Voltage at the inverter side	(V)
ω	Angular frequency	(rad/s)

x	x position in the Cartesian coordinate system	(m)
y	y position in the Cartesian coordinate system	(m)
z	z position in the Cartesian or cylindrical coordinate system	(m)
Z_C	Cable impedance	(Ω)
Z_M	Motor impedance	(Ω)
Z_S	Inverter impedance	(Ω)

Chapter 1
INTRODUCTION

1.1 Preface

It is obvious that energy is one of the most vital problems in the world. Along with the attempts of using renewable energies from wind, the sun, etc. to replace the polluting and exhausting fossil fuels, it is essential to enhance the efficiency in power consumption. In practice, using adjustable speed drives (ASDs) to control AC motors is one successful solution for the above issue. The configuration of this technology is illustrated in Fig. 1-1. The converter receives electrical energy from a power frequency grid and converts this energy to a frequency-variable one that feeds the motor, hence, the rotational speed of this motor can be controlled. Over the past ten years, the demand for these ASDs has been growing, especially at medium voltage rate (above 600V), in many applications, for examples, rolling mills, extraction pumps, etc [1]. This trend is also a challenge for the insulation structures of motors because of the presence of repetitive impulses in the output voltage of ASDs. Hence, searching for designs of insulation systems that are compatible to inverter-fed motors is an inevitable demand. The following section is written to explain some basic features of stress grading systems in the insulation of rotating machines.

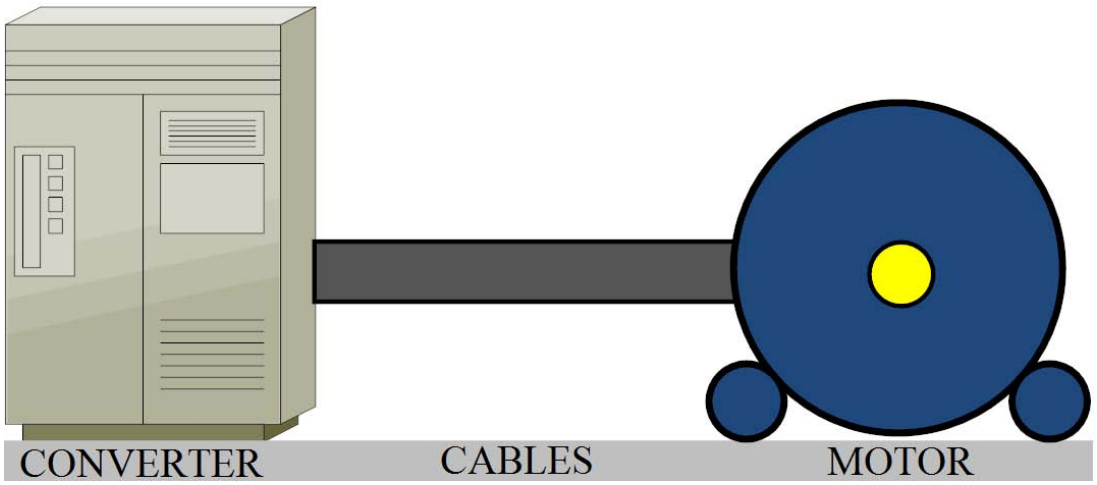

Fig. 1-1: *A general configuration of inverter-driven motor.*

1.2 Stress grading system structure

In IEC Technical Specification (TS) 60034-18-42, type II form wound insulation system is used in electric motors of rate voltage above 700 V and it is defined to withstand partial discharge (PD) during its life-time [2]. Besides, a stress grading system (SGS) consisting of a conductive armour tape (CAT) and a semiconductive tape (SCT) is required to reduce the surface electrical stress in case of voltage above 5kV [3]. This type of insulation structure is described in Fig. 1-2.

1.2.1 Conductive armour tape

Inside the stator slot, to give a good electrical contact between the surface of the main insulation and the stator laminations, a CAT is used and it extends a few centimeters outside the stator slot as illustrated in Fig. 1-2 [4]. This tape is commonly a composite of either varnish or polyester resin with graphite or carbon black [4]. The electrical resistivity of this tape is required to be small enough to suppress PD inside the slot but not too low as to increase eddy currents through the stator laminations [5]. In the manufacture of motors, the insulation of

stator coil is cured using vacuum pressure impregnation (VPI) or resin-rich technologies, and the conductivity of the CAT can decrease by over 100 times [6]. The suitable electrical conductivity of this material is supposed to be from 10^{-5} to 10^{-2} S/m [7].

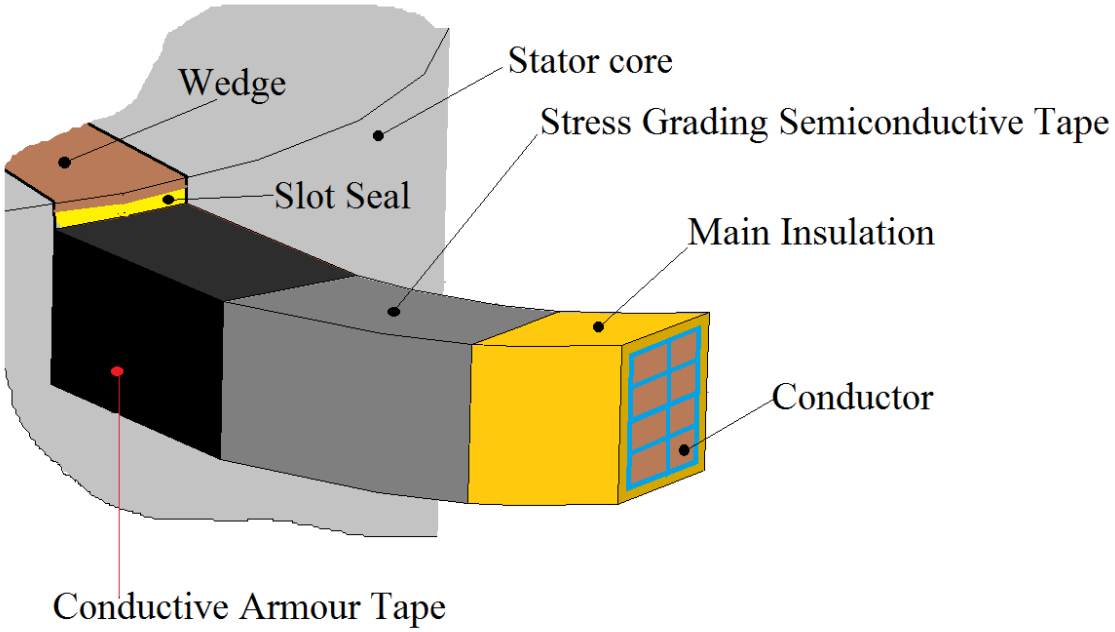

a) 3D view

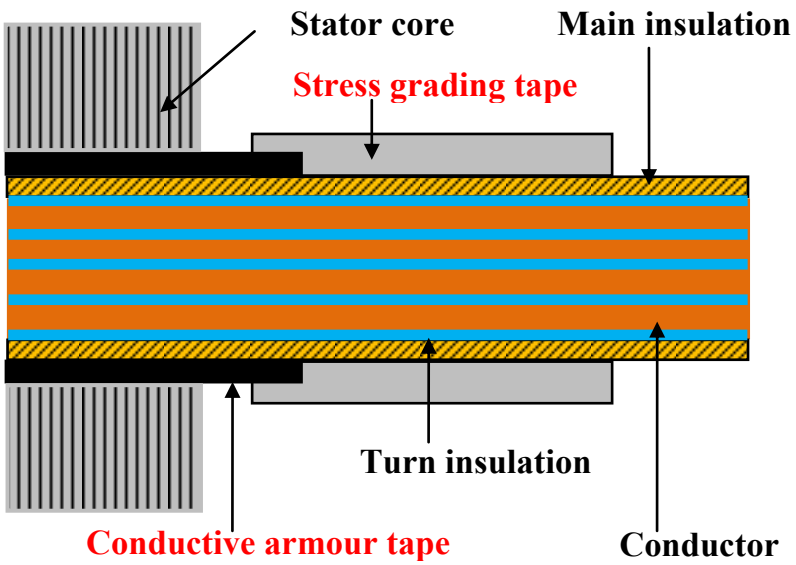

b) 2D view along the axis of stator coil

Fig. 1-2: *A typical structure of type II form wound insulation system.*

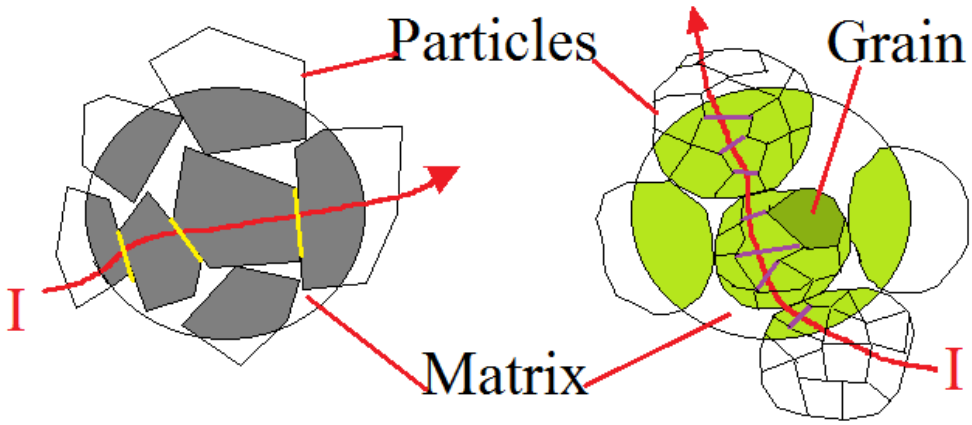

a) SiC b) ZnO microvaristors

Fig. 1-3: *Microstructure view of semiconductive materials based on SiC and ZnO* [8].

1.2.2 Semiconductive tape

At the end of the CAT, a SCT is used to give a smooth transition from the low potential on the CAT to the high one on the outside main insulation [4]. For production of SCT, manufacturers use composite materials in which one or more specific fillers are mixed into the insulation matrixes with the quantity higher than the percolation threshold and, hence, the particles of these fillers can provide continuous and conducting paths through the composites [8].

The most important property of these materials for stress grading is their field dependent electrical conductivity. Based on the mechanism of semiconducting, these materials can be classified into two particular groups, traditional and new ones. The former includes polymeric composites with extra fillers such as silicon carbide, carbon black, and some metal oxides, etc. In commercial market, the most favorite filler is silicon carbide (SiC) because of its superior properties for thermal and mechanical performances [9]. The second

group is based on microvaristor fillers with a typical example of Zinc Oxide (ZnO). The origin of the nonlinear electrical conductivity of the two categories can be explained based on the micro-view at the two typical examples of SiC and ZnO based SCTs in Fig. 1-3. In the first example, thin interfacial oxide layers are spontaneously formed between two adjacent SiC particles (the yellow lines in Fig. 1-3a). Through these surfaces, electrons or holes move from one particle to the neighbor either by hopping, tunneling, thermal activation or by combination ways over the potential barriers, similar to Schottky barriers in normal semiconductors [8]. Obviously, the nonlinear electrical conductivity of the traditional materials is originated from this transport mechanism through the interfaces between two neighboring particles. Therefore, the nonlinearity of materials in the first group is quite sensitive to many environmental parameters such as pressure, wear, humidity, etc [8]. In the second category, the nonlinearity is decided by the inside structure of each ZnO particles. As illustrated in Fig. 1-3b, each ZnO particles consist of many micrometer-sized grains, and hence, double Schottky barriers are formed at each grain boundaries (brown lines) [8]. The electrically active boundaries, which are n-i-n type semiconductor junctions, serve the nonlinearity of materials in this group [8].

1.3 Temperature and field dependence of materials in stress grading systems

In general, under a sinusoidal field with the angular frequency ω (rad/s), the permittivity of dielectric materials is displayed in a complex number form as (1-1).

$$\varepsilon = \varepsilon' - j\varepsilon'' \quad \text{(1-1)}$$

In (1-1), the real component ε' relates to the charging current in an ideal capacitor while the imaginary one ε'' is involved in the dielectric loss [10].

The Maxwell-Ampere equation in these materials is displayed in the frequency form as (1-2); where $\vec{H}$ (A/m) and $\vec{E}$ (V/m) are the magnetic and electric field intensities, σ_{DC}(S/m) is the electrical conductivity of the materials in the static electric field condition.

$$\nabla \times \vec{H} = \sigma_{DC}\vec{E} + (\varepsilon' - j\varepsilon'')j\omega\vec{E} \quad \text{(1-2)}$$

Equation (1-2) is transformed as follows

$$\nabla \times \vec{H} = (\sigma_{DC} + \omega\varepsilon'')\vec{E} + \varepsilon' j\omega\vec{E} \quad \text{(1-3)}$$

From (1-3), the total conductivity of the materials under a sinusoidal field is defined in [10] as

$$\sigma_{ec} = \sigma_{DC} + \omega\varepsilon'' \quad \text{(1-4)}$$

Based on (1-4), the total conductivity of the materials can be considered as a function of electric field frequency, electric field strength and temperature in a general form as follows

$$\sigma_{ec} = f(\omega, E, T) \quad \text{(1-5)}$$

In order to get the electrical conductivity profiles of CAT and SCT, measuring samples, which have to be prepared and treated through a VPI process in accordance with type II insulation of stator coil in the practical manufacture of motors, are displayed in Fig. 1-4 [11].

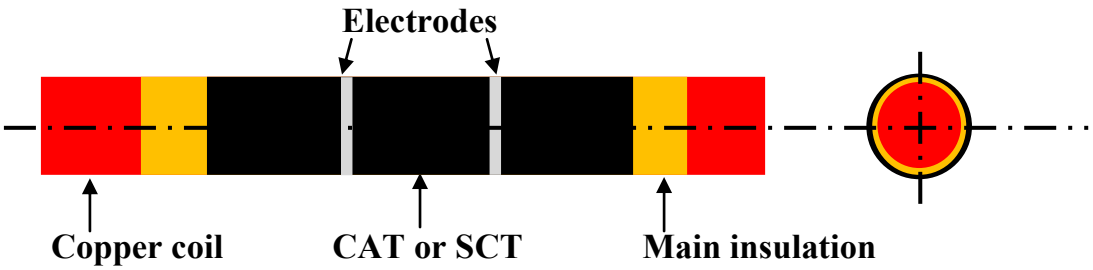

Fig. 1-4: *Measuring samples of CAT or SCT in* [11].

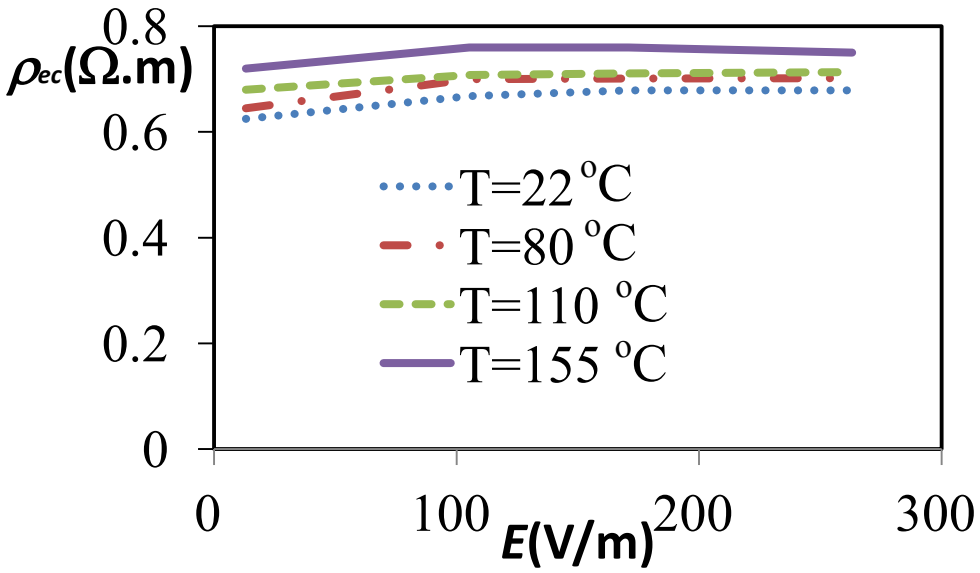

Fig. 1-5: *DC resistivity of CAT measured at 22 °C, 80 °C, 110 °C and 155 °C in* [11].

In [11], the electrical resistivity profiles of these tapes are measured under DC conditions using the measuring samples in Fig. 1-4. The resistivity of CAT versus the electric field strength at 22 °C, 80 °C, 110 °C and 155 °C are obtained as some typical curves as in Fig. 1-5. It is realized that the electrical conductivity of CAT is verified having a little dependence on the applied electric field strength and temperature, hence, this parameter of CAT can be considered as a constant value. On the other hands, based on the changing curves of the

resistivity versus the electric field strength illustrated in Fig. 1-6, the electrical conductivity of SCT is demonstrated to have a considerable dependence on the temperature, and a strong one on the electric field strength.

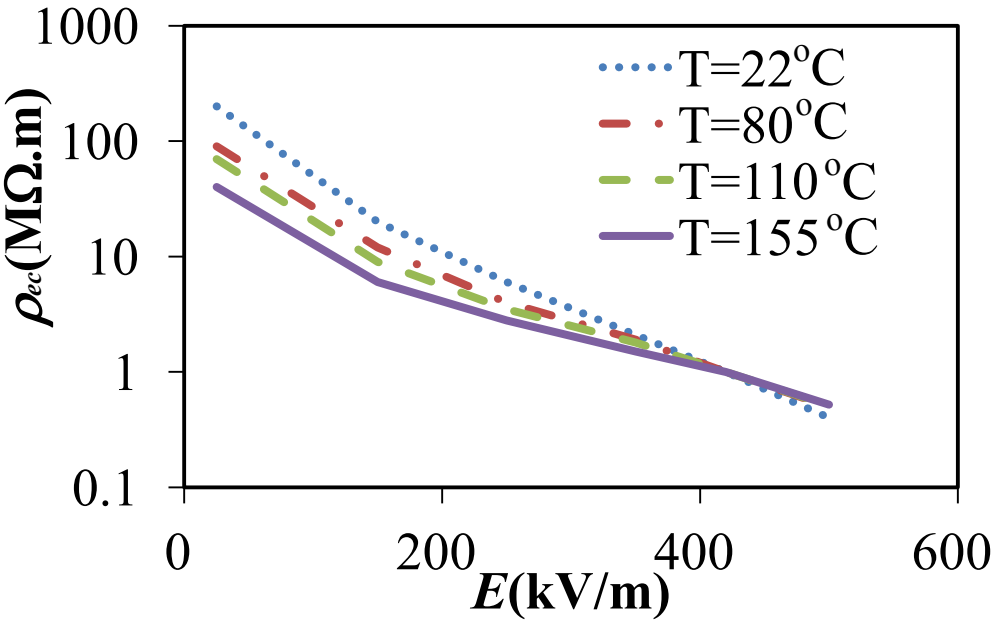

Fig. 1-6: *DC resistivity of SCT measured at 22* °C, *80* °C, *110* °C *and 155* °C *in* [11].

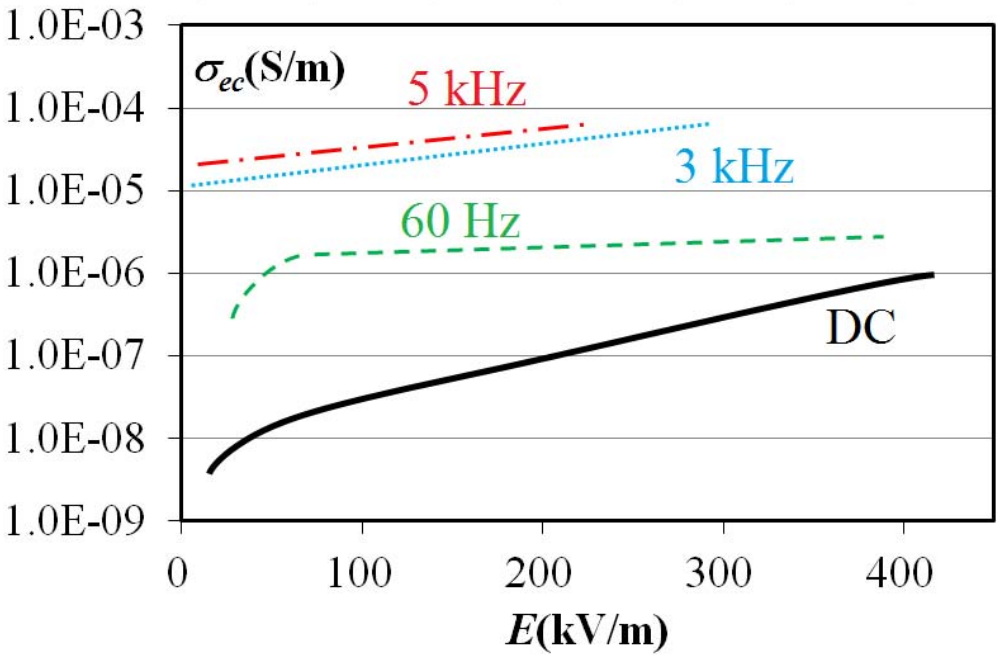

Fig. 1-7: *Electric field dependent curves of the electrical conductivity of SCT measured at DC, 60* Hz, *3* kHz *and 5* kHz *in* [12].

To verify the effect of frequency to the dielectric parameters of CAT and SCT, a high voltage and high frequency measurement system is developed in [12]. All the measurements are conducted at the temperature of 20 ^{o}C for both CAT and SCT. From the measurement results in [12], the electrical conductivity of the CAT is clarified being independent of the applied frequency up to 2 MHz. In contrast, the frequency is confirmed having a significant influence on the electrical conductivity of the SCT. Fig. 1-7 outlines the SCT electrical conductivity as functions of electric field strength in four typical cases of DC, 60 Hz, 3 kHz and 5 kHz. It is observed that the nonlinear variation of the SCT conductivity versus the electric field strength decreases with the increase of the frequency [12]. As a result, although this parameter of SCT increases with the frequency, the stress grading ability of this tape can be reduced seriously.

1.4 Literature review

The purpose of this section is to give a general view and trend of previous researches which have significant contributions in enhancing the working ability of SGSs used in inverter-fed medium voltage motors.

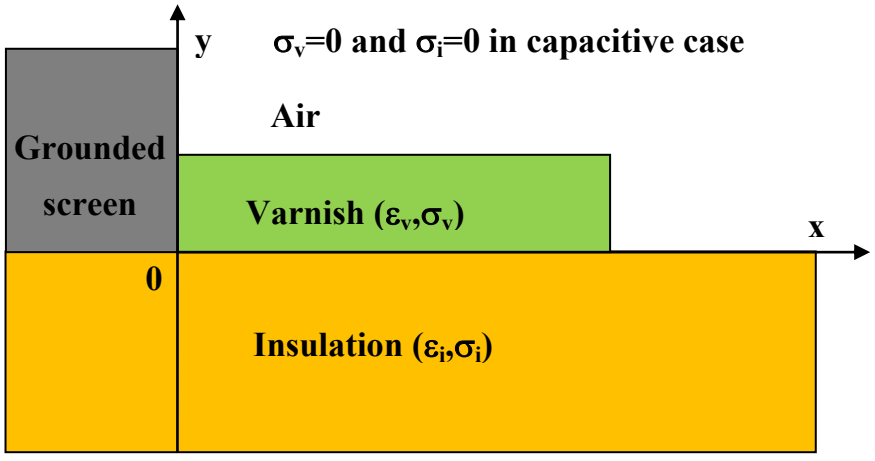

Fig. 1-8: *A typical stress grading configuration for optimization problem in [13].*

First of all, it is necessary to mention about the design and optimization problem of SGSs working under sinusoidal voltage sources. This classical topic was a hot theme in the past due to a strong increase in using rotating machines in the industry from all over the world. Jean P. Rivenc and Thierry Lebey summarized this attracting research field in [13]. In this overview, two classified types of materials are distinguished from each other using a definition: capacitive material if $\sigma_{ec} < \varepsilon\omega$ and resistive one if $\sigma_{ec} > \varepsilon\omega$. A general optimization problem of reducing the electric field in a typical configuration applied under 15 kV and 50 Hz sinusoidal voltage as in Fig. 1-8 was considered. The solution of using a capacitive varnish of either constant permittivity or nonlinear permittivity materials was verified to be not satisfactory. Besides, resistive materials of electrical conductivity around the value of 10^{-5} S/m provided a satisfactory solution for reducing electric stress in the configuration at the industrial frequency of 50 Hz or 60 Hz. Some experimental results with nonlinear materials were mentioned to support the idea that these nonlinear materials could not provide a good stress grading effect, and hence, a pessimistic conclusion was drawn from this research that is "The nonlinear behavior does not seem to be the required property for stress grading optimization" [13]. However, with the rapid development of material science, applications of materials with a nonlinear field dependent property have become more and more important in stress grading design and optimization. Therefore, many studies have been attracted in this topic.

In 2002, A. E. Baker et al. [14] developed a finite element method (FEM) model to analyze the electrical nonlinear-behavior of materials for end windings of rotating machines. In this model, field dependent electrical property of the SCT was considered as a surface element without physical thickness and

formulated under a form of surface electrical resistivity $\rho_S = K \cdot exp\left(-nE^{\frac{2}{3}}\right)$ [14]. Emad Sharifi et al. [11] addressed the temperature dependent electrical conductivity of tress grading materials in form-wound end-winding coils. Electrical conductivity of CAT and SCT were measured at some typical temperatures up to 150 ^{o}C, and then inputted into a 2D-FEM model to compute electric field stress in stress grading samples under power frequency sinusoidal voltages. In addition, in order to verify the computation results, a measurement system was setup to record the electric potential distribution on examined SGSs with a space resolution of 1mm using an electrostatic voltmeter. Christian Staubach et al. [15, 16] presented a multiple-coupled FEM model which can analyze electric field and thermal stresses in a 3D structure of SGS for large rotating machines at power frequency. Then particle swarm based simplex optimization method was proposed using the above FEM model in frequency domain to obtain an optimal design of the considered stress grading configuration.

Until the time this thesis written, the problem of optimization and design for SGSs under power frequency sinusoidal supplying sources was solved successfully and these end-winding stress relief structures have been under effective working conditions. However, the use of inverter to drive motors, especially at medium voltage pushes SGSs into tough situations. Hence, analyzing and designing for this important structure working in these inconvenient conditions are inevitable demands.

In 2005, Jeremy C. G. Wheeler [17] laid the groundwork for this topic using the FEM model in [14] to compute electric potential and electric field stress distribution along the surface of SGSs under 50 Hz, 2 kHz and 250 kHz sinusoidal voltage sources. From this analysis, high electric field stress data were

recorded for the cases of the high frequency sources and surface discharge being supposed to occur. Experiments for stress grading samples energized by converter voltages were carried out to verify the computation results and to confirm that surface discharge can develop at the stress level of 450V/mm. Besides, high temperature rise was recorded by infrared cameras in these laboratory tests.

In the same year, Fermin P. Espino-Cortes et al. [4] proposed a FEM model to calculate the surface electric field stress on a conventional stress grading structure under a transient voltage with the fast rise time of 200 ns and an overshoot value of around 18 kV. The simulation results show that high electric field stress is located on the CAT near the stator slot exit during the rise time of the applied voltage. A solution using a higher electrical conductive part of CAT outside the stator slot was suggested and verified by simulation. Besides, a validating experiment using stress grading structures applied under an impulse voltage from a pulse generator with the same rise time of 200 ns and a repetition at 100 pulses every second was conducted. Images from infrared cameras were used to locate PD positions which suffered high electric field stress on the experimental stress grading structures.

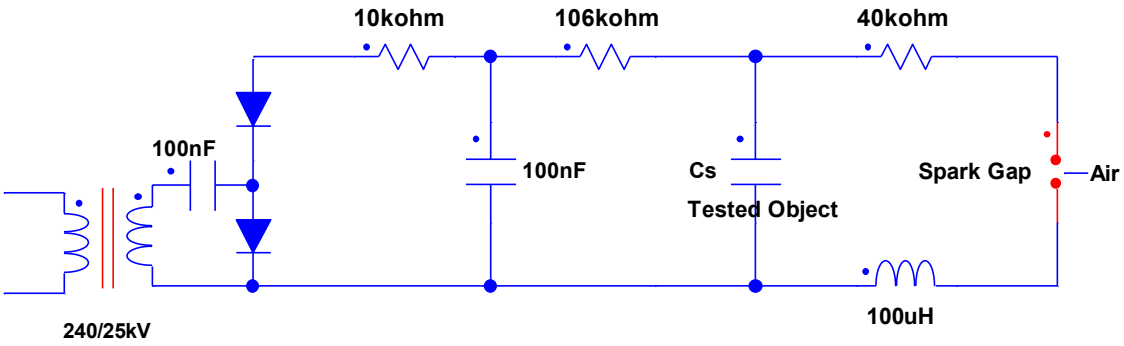

Fig. 1-9: *Spark gap generator circuit proposed in* [18].

A further research was carried on by Jeremy C. G. Wheeler et al. [18]. In this attempt, a laboratory low cost impulse generator whose general circuit is described in Fig. 1-9 was proposed to replace expensive inverters and used to test two-layered, sleeved designed stress grading samples. The experimental results showed that the electric field stress on the surface of end-winding SGSs under inverter sources is much higher than the one under 50 Hz or 60 Hz sinusoidal voltage sources, and the double layered sleeved structures can be an efficient solution for SGSs in inverter-fed motors.

Another effort to improve the performance of SGSs under inverter sources was conducted by Fermin P. Espino-Cortes et al. [19]. A sectionalized stress grading structure illustrated in Fig. 1-10 was proposed and demonstrated to be effective by both simulation and experiments: high electric field stress is pushed to move far away from the stator slot exit and it is located on the second conductive tape during the front time of the applied impulse and on the SCT at the remain time.

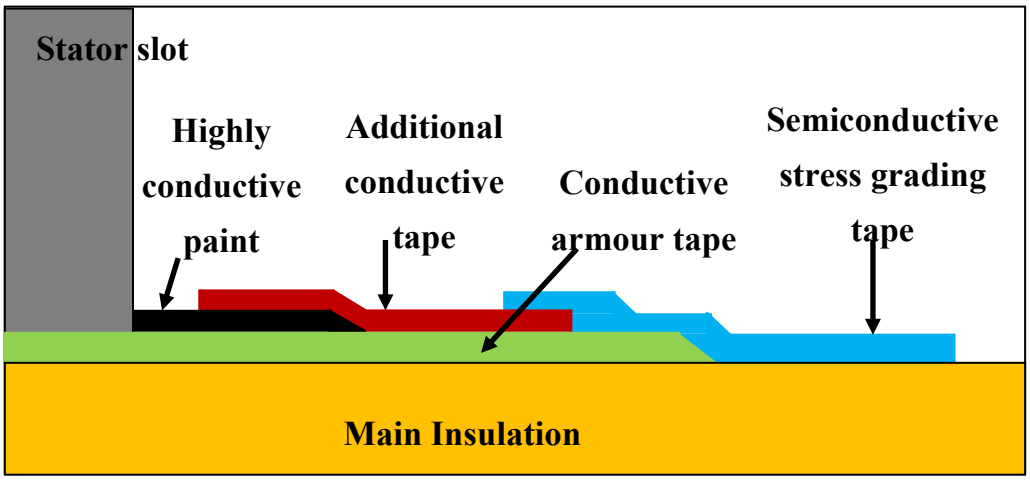

Fig. 1-10: *Sectionalized structure of stress grading system with an additional conductive tape in [19].*

Jeremy C. G. Wheeler et al. [20] focused their research on the changes of nonlinear electrical conductivity of SCTs under different temperature conditions. An aging process of three market-available SCTs up to 155°C was developed, and surface electrical resistivity of these samples was measured at room temperature (around 20 °C), 90 °C, 105 °C, 130 °C and 155 °C. The surface resistivity of all tested semiconductive samples was recorded being reduced, and one of these tapes almost lost its nonlinear property at 155 °C but restored this characteristic after one aging cycle of more than 16 hours. Returning to the room temperature, the resistivity of two tapes became much higher than its original value while the one of the third tape almost remained the same as before testing.

In order to support the development of a new IEC TS guideline of SGS in ASD medium voltage machines, William Chen et al. [21] applied the impulse generator proposed in [8] to make a qualification test for stress grading structures using several different conductive tapes. The measurement results showed that the available stress grading standard designs had to be replaced by new ones designed for inverter-fed motors.

In 2008, IEC/TS 60034-18-42 [2] was published based on many efforts of experts from around the world. Important contributions to this guideline were mainly based on researches in [4, 17-18, 20]. It provides criteria for assessing type II insulation systems used in voltage source inverter fed motors.

E. Sharifi et al. proposed some capacitive stress grading structures for voltage source inverter conditions [22-23]. To replace the stress relief ability of SCTs, embedded conductive foils were installed inside the main insulations of SGSs as illustrated in Fig. 1-11. These improvements were demonstrated to be effective in electrical and thermal stress grading under fast impulse voltages

using both FEM analysis and IEC qualification test. However, their complicated structures with conductive foils inserted in the main insulation are tough obstacles for practical production.

In 2010, E. Sharifi et al. [12] introduced an AC model using anisotropic dielectric properties of materials in SGSs. A measurement system using a high voltage and high frequency transformer was set up to collect these anisotropic parameters. The AC model was supposed to have a higher accuracy than the one based on DC isotropic profiles of materials, especially in the case of very high electric field conditions. Around this time, the thermal performance of SGSs under a unipolar 2-level pulse width modulation (PWM) voltage sources, at the first time, was analyzed by a 2D FEM model in [24] and then by an improved 3D FEM model in [25]. In these models, the stationary mode of coupled electro-thermal study was used to analyze the thermal behavior of the examined SGS under two sinusoidal voltage sources of 5 kHz and 50 kHz. The frequency and amplitude of the two sources were determined by a process of "trial-and-error". The superposition of thermal effects caused by the two voltages was verified to be the same as the one of the studied voltage by a laboratory experiment.

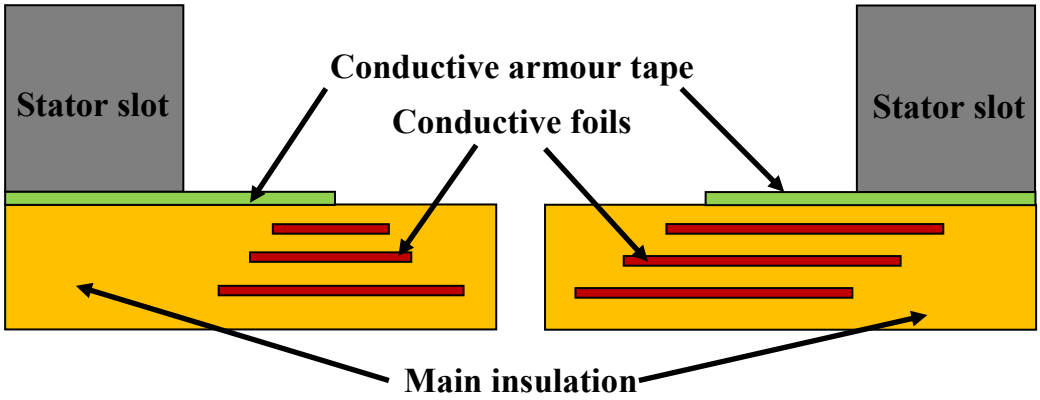

a) proposed in [22] b) proposed in [23]

Fig. 1-11: *Illustration of capacitive stress grading systems using embedded foils.*

Another research on thermal performance of SGSs under inverter sources was conducted based on an equivalent circuit model by F. P. Espino-Cortes et al. in [26]. However, this model cannot give a detailed thermal analysis of SGS because neither the physical thickness dimension nor the heat transfer process is considered.

For electrical stress relief performance assessment of SGSs, the electric potential distribution on the surface of these structures is a very important profile. Electrostatic voltmeters are used to measure this parameter in case of power frequency sinusoidal voltage source. However, in fast impulse conditions, these traditional measurement devices cannot be applied because the applicable frequency is limited in the range from DC to around 100 Hz [22]. Therefore, a new measurement method is an essential requirement. A. Kumada et al. [27] and K. Kiuchi et al. [28] applied an optical system based on Pockels effect to measure the potential distribution on the surface of SGSs under fast impulse voltages such as 1 kHz rectangular one. This measurement was continued for a fast impulse with a rise time of 250 ns in coordination with a PD detection system using an intensified charge-couple device (ICCD) camera by T. Nakamura, et al. [29]. An interesting result in this experiment is that PD is detected in the middle part of the CAT where the surface electric gradient is supposed to be low.

1.5 Objective of the present study

From the literature review, it is noted that there are some issues of SGSs needed to be clarified. The most important one is the working mechanism of SGSs under PWM voltages of multi-level inverters which still remains unclear. In addition, it is supposed that a difficult and impractical problem is the transient analysis of the thermal process inside SGS structures directly under high

repetitive and fast impulses of PWM voltages [24]. Hence, the final target of this research is to develop two simulation models that can analyze the electrical and the thermal processes inside the SGSs of medium voltage motor under not only PWM voltage but also all waveform ones. Besides, for the improvement designs of SGSs, these models can be used in the preliminary stage before testing real structures of SGSs in laboratories.

1.6 Thesis outline

1.6.1 Chapter 2: Modelling

At the beginning of this chapter, there would be a brief overview about approaches applied for the SGS analysis. Then two main models of electric field and heat transfer analyses of the SGS built in COMSOL Multi-physical program would be explained. Finally, two extra models of multi-level Series Connected H-bridge Voltage Source Converter (SCHB VSC) and PWM surge travelling developed in Matlab/Simulink would be presented.

1.6.2 Chapter 3: Results

This chapter is designed to present all the computation results provided by the above analysis models. The electrical and thermal analyses of the SGS under sinusoidal voltages with the frequency range from 50 Hz to 5 MHz would be conducted to provide a basic frequency response of this insulation structure. These analyses would then be carried out for the cases of PWM voltages from the two multi-level converters. At the end of this chapter, the impact of overshot voltage caused by the cable-motor impedance mismatch on the working ability of the SGS would be studied. Based on these obtained results, not only the electrical

stress grading mechanism but also the thermal process inside the SGS would become clear.

1.6. 3 Chapter 4: Discussion

The mechanisms of the electrical and thermal stresses in the SGS would be explained based on the computation results in Chapter 3. After that, the validation of our models is conducted by comparing our computation results with some experimental ones of other researchers.

1.6.4 Chapter 5: Conclusion and future works

This chapter concludes the remarkable contributions of the research study. Besides, some important problems would be discussed for the next studies on the SGS design.

Chapter 2
MODELLING

2.1 Approaches applied for stress grading analysis in previous works

For analysis of SGSs in rotating machines, three typical methods already used in previous works are equivalent circuit, conformal mapping and finite element. The following contains a brief summary for these methods.

Firstly, equivalent circuit is a classical method in which semiconductive stress grading tapes are presented by a series of nonlinear resistances while parallel capacitances are used to replace for main insulation layers. These circuit elements can be calculated based on the real design of stator coils. Hence, an insulation structure can be simplified as the equivalent circuit in Fig. 2-1. There are two popular techniques to solve this nonlinear circuit. The first one is using mathematical tools such as Matlab to compute a nonlinear system of differential equations derived from Kirchhoff's laws [30-31]. The other choice is using a commercial program of circuit analysis, for instance PSCAD/EMTDC [26]. This method can provide basic profiles of surface potential distribution [30-31] and resistive heat density [26] along the axis of the stator coil. Although this method is easily applied, its solution is not accurate because of many simplifications, especially the ignored effect of physical thickness of the insulation structure [26].

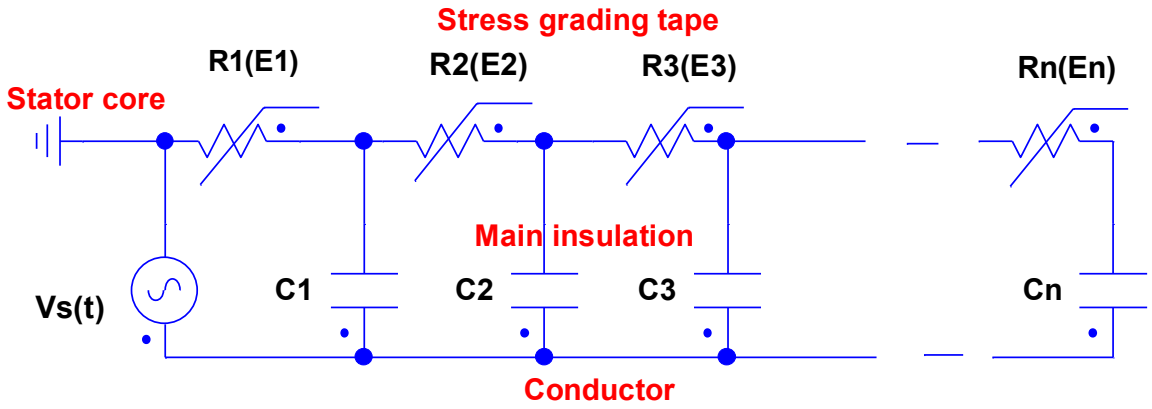

Fig. 2-1: *Equivalent circuit of a stress grading system* [26,30-31].

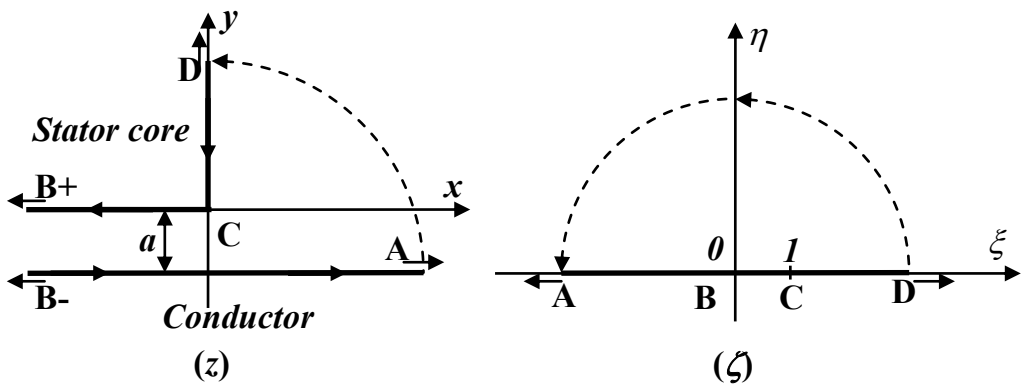

Fig. 2-2: *Schwarz-Christoffel conformal transformation mapping plane* (z) *onto plane* (ζ) [13, 32].

Secondly, when the electrical conduction is neglected, conformal mapping can be used to provide the equipotential equations analytically in the theme of potential distribution governed by Laplace's equation $\nabla^2 V = 0$ [32]. Rivenc et al. [13, 32] applied Schwarz-Christoffel conformal transformation to map the inside homogeneous medium between the stator core and the conductor, plane (z) onto the semi-infinite half-plane (ζ) as in Fig. 2-2. It is noted that the potential is zero on the segments B+CD and is V_s, voltage applied between the conductor and the grounding stator core on the segment AB [32]. Finally, the position equations of the equipotential lines can be expressed as equations (2-1) and (2-2), where V is

the electrostatic potential and F is the electrostatic flux. Based on these equations, for a specific value of V in the range from 0 to V_s, an equipotential line can be obtained by changing the value of F [13, 32]. In a SGS consisting of many different materials, the above procedure can be modified to take into account the presence of different media using the electric field boundary conditions [13, 32]. In case a highly conductive tape is used and the electrical conduction cannot be ignored, this conformal method can also be applied with a support of the equivalent circuit method [13, 32]. However, this analytical method cannot be applied for practical applications using semiconductive stress grading tape and high frequency voltage sources.

$$x = x(V, F) \quad \text{(2-1)}$$

$$y = y(V, F) \quad \text{(2-2)}$$

These two methods mentioned above have many disadvantages for solving the stress grading problem of practical insulation structures in rotating machines, and hence they are no longer attractive. Meanwhile, FEM is a suitable choice for this problem because of its flexibility for handling nonlinear materials and very thin layers. Hence, many researchers have been developing their own FEM programs to analyze this problem [14, 15-17, 33]. Besides, many FEM based software packages such as COMSOL, ANSYS, ALGOR, etc. have bloomed on the market recently. These commercial programs provide not only many specific modules for numerous fields of engineering but also customer-friendly interfaces. Therefore, applications of these powerful tools are more and more popular. Many studies have used COMSOL to analyze the electrical and the thermal performances of SGSs in inverter-driven motors [4, 11-12, 19, 22-26].

In the same trend, this work for non-linear analysis of the electrical and the thermal SGSs is conducted mainly based on COMSOL. The detailed analysis models are introduced in the following sections.

2.2 FEM based models of stress grading system

2.2.1 Electric field analysis model

Firstly, it is necessary to reintroduce the most popular equations in the electromagnetic field theory, Maxwell's equations applied for this nonlinear problem as expressed in equations (2-3) and (2-4). In these equations, $\vec{E}$ (V/m), $\vec{D}$ (C/m^2), $\vec{H}$ (A/m) and $\vec{B}$ (Wb/m^2) are the electric field intensity, the electric flux density, the magnetic field intensity and the magnetic flux density, respectively while σ_{ec}(S/m) is the electrical conductivity.

$$\nabla \times \vec{E} = -\frac{\partial \vec{B}}{\partial t} \quad \text{..... (2-3)}$$

$$\nabla \times \vec{H} = \sigma_{ec}\vec{E} + \frac{\partial \vec{D}}{\partial t} \quad \text{..... (2-4)}$$

The size of SGSs is small compared to the wavelength of the electromagnetic field in these structures and the energy in the magnetic field is much smaller than that in the electric field [33]. Hence, the induced current ($-\partial\vec{B}/\partial t$) can be neglected, equation (2-3) becomes $\nabla \times \vec{E} = 0$. This means that the electric field $\vec{E}$ can be presented by a scalar potential V as (2-5).

$$\vec{E} = -\nabla V \quad \text{..... (2-5)}$$

Besides, derived from the equations: $\nabla \cdot \left(\nabla \times \vec{H}\right) = 0$, $\vec{D} = \varepsilon \vec{E}$ with ε (F/m) is the electric permittivity, (2-4) and (2-5), the transient electric quasi-static equation is finally obtained as follows

$$-\nabla \cdot \left[\sigma_{ec} \nabla V + \frac{\partial(\varepsilon \nabla V)}{\partial t}\right] = 0 \quad \text{(2-6)}$$

To analyze the electrical performance of SGSs governed by equation (2-6), Electric Current mode in AC/DC module of COMSOL is chosen. For SCTs, as discussed in chapter 1, the electrical conductivity is a field and temperature dependent parameter described in term of $\sigma_{ec}=f(\omega, E, T)$. This nonlinear property of SCTs is extremely complicated to take into account in the electric transient analysis. In order to overcome this barrier, an electrical conductivity profile of SCTs in a typical condition with specific values of frequency and temperature is used in analysis. In this case, this parameter can be considered as a function which is only dependent on the electric field strength $\sigma_{ec} = f(E)$.

During electrical stress grading, the electric field stress mainly orients along the axis of SGSs. Hence, it is reasonable to use a cylindrical stator end-winding insulation structure for analysis of this phenomenon. Beside, this application can avoid an extremely high memory cost in the case of 3D computations. The detailed structure of this SGS in 2D axially-symmetric coordinate (*r-z*) is illustrated in Fig. 2-3. The stator copper coil is assumed to have a round cross section with a radius of 10 mm. The main insulation applied over the coil with a thickness of 2.4 mm is made from a mica based tape. The thickness of the CAT and that of the SG semi-conductive layers are 0.5 mm and 0.7 mm, respectively. The electrical properties of these materials which are summarized in Table 2-1 are assumed to be independent of temperature. Besides,

the DC electrical conductivity of the SCT, which has a nonlinear relationship with the applied electric field strength, is referred in [11] and compared with the ones of the other materials in Fig. 2-4.

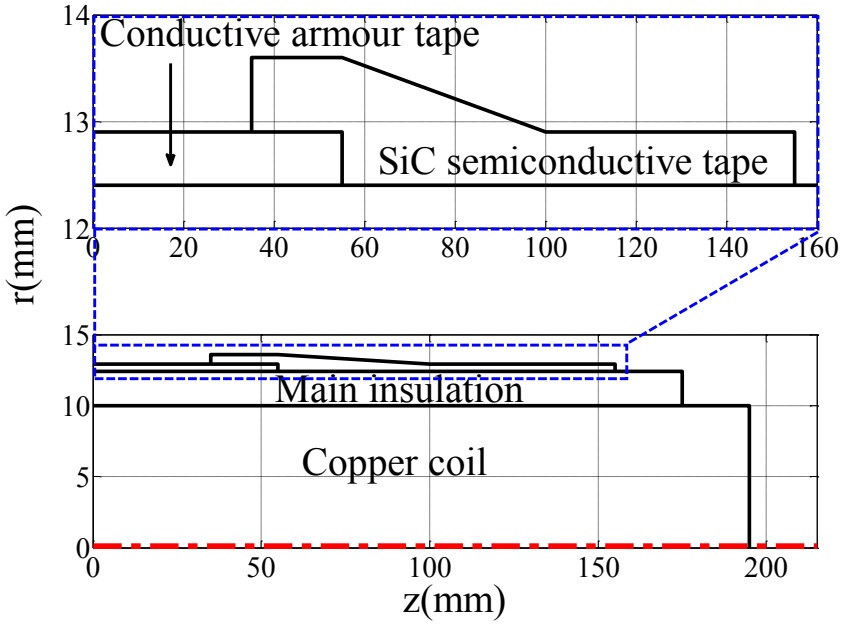

Fig. 2-3: *Detailed size of the studied stress grading system in 2D axially symmetric coordinate (r, z).*

Table 2-1: *Electrical properties of the materials.*

	Materials	***Electrical conductivity*** σ_{ec} ***(S/m)***	***Relative permittivity*** ε_r
1	Copper	5.998×10^{7}	1
2	Main insulation	2.01×10^{-15}	4
3	CAT	0.01	20
4	SiC SCT [11]	$\frac{1}{5.4\times10^{8}}e^{0.00112E^{\frac{2}{3}}}$	20
5	Air	10^{-18}	1

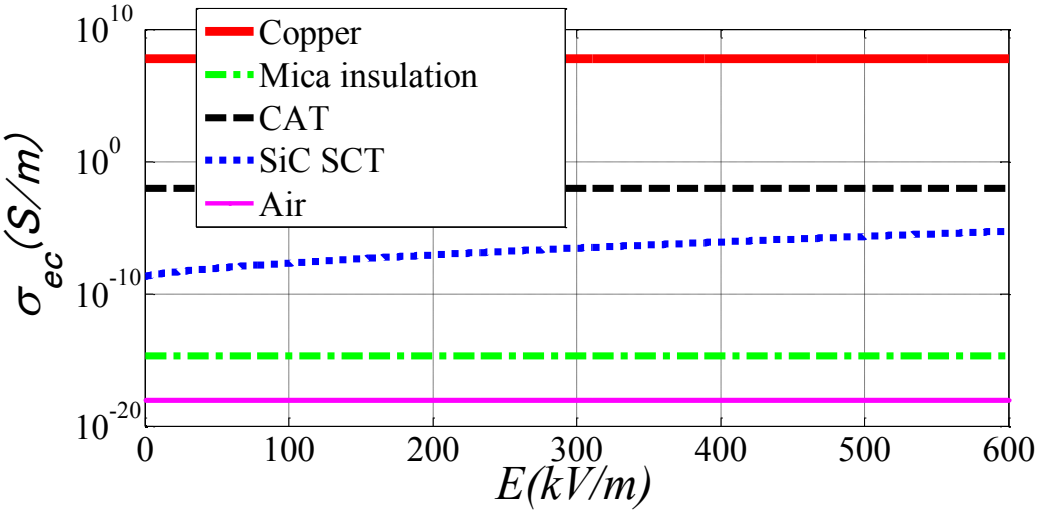

Fig. 2-4: *Electrical conductivity of the materials versus electric field strength.*

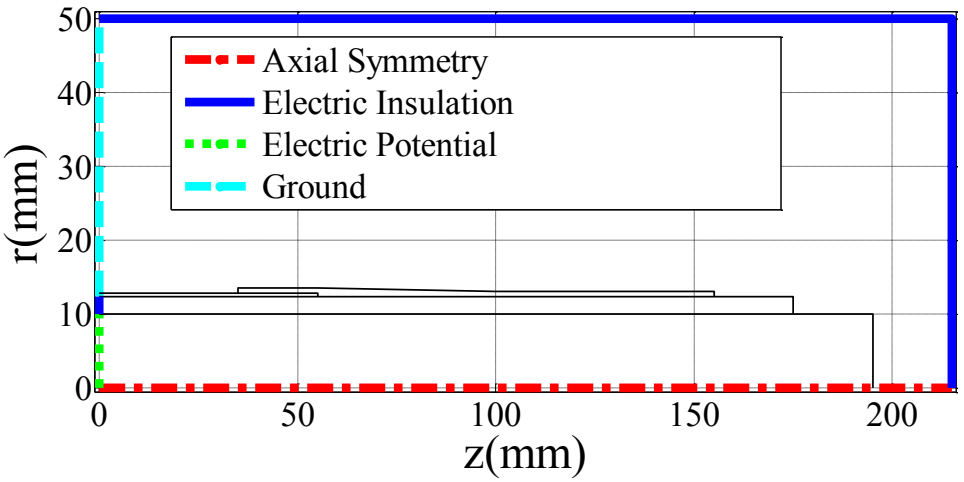

Fig. 2-5: *Boundary conditions used in the electric field analysis model.*

In this FEM based analysis, boundary conditions have to be determined at the covering frontiers of the computed domain. Fig. 2-5 displays the boundary conditions applied in this model. The ground boundary condition is applied with zero potential while the electric potential one is assumed to be the applied voltage source. Besides, the electric insulation boundary condition is based on equation (2-7), in which $\vec{n}$ and $\vec{J}(\mathrm{A/m^2})$ are the unit normal and the electric current density vectors.

$$\vec{n} \cdot \vec{J} = 0 \quad \text{(2-7)}$$

2.2.2 Heat transfer analysis model

The temperature T (K) in the SGS is calculated relying on equation (2-8), in which ρ (kg/m^3), $\vec{u}$ (m/s), C_p (J/(kg·K)), k (W/(m·K)) and Q (W/m^3) are the mass density, the velocity vector, the heat capacity, the thermal conductivity and the heat source density, respectively [34]. The second term on the left of this general equation is ignored in case of solid materials. The other thermal parameters of the materials are assumed to be independent of temperature and shown in Table 2-2.

$$\frac{\partial(\rho T)}{\partial t} + \nabla \cdot (\rho \vec{u} T) = \nabla \cdot \left(\frac{k}{C_p} \nabla T \right) + \frac{Q}{C_p} \quad \text{(2-8)}$$

To determine the dissipated power causing heat generation in a SGS under an electric field, it is necessary to mention the integration form of Poynting theorem achieved for a volume VD inside a close surface S as follows.

$$-\oiint_S \vec{P} \cdot d\vec{s} = \iiint_{VD} \left(\sigma_{ec} \vec{E} \cdot \vec{E} \right) dv + \iiint_{VD} \left[\vec{E} \cdot \frac{\partial(\varepsilon \vec{E})}{\partial t} \right] dv \quad \text{(2-9)}$$

Table 2-2: *Thermal properties of the materials.*

	Materials	***Mass density*** ρ **(kg/m^3)**	***Heat capacity*** C_p **(J/(kg·K))**	***Thermal conductivity*** k **(W/(m·K))**
1	Copper	8700	385	400
2	Mica	208	500	0.71
3	CAT	900	800	0.19
4	SiC SCT	900	800	0.19

In (2-9), $\vec{P}$ (W/m^2) is the Poynting vector and the first volumetric integration is the dissipated power inside the volume *VD*, and it causes the heat generation in this volume [35-36]. The second volumetric integration of (2-9) is the exchanging power of the electric energy in the volume *VD* [36].

From (2-9), the dissipated power density Q_{res} (W/m^3) can be extracted as in (2-10) and considered as a heat source density at each positions inside the volume *VD* for the heat transfer analysis.

$$Q_{res} = \sigma_{ec}\vec{E}\cdot\vec{E} = \sigma_{ec}\left|\nabla V\right|^2 \quad \text{(2-10)}$$

In this heat transfer analysis model, the average dissipated power density $\bar{Q}_{res}$(W/m^3) can be determined using equation (2-11), and then considered as a constant heat source density in the general equation (2-8). In this study, with the fundamental frequency of 50 Hz, t_0 = 10 ms from the beginning of the second duty cycle (at least), and $\Delta\tau$ =10 ms are chosen for computing.

$$\bar{Q}_{res} = \frac{1}{\Delta\tau}\int_{t_0}^{t_0+\Delta\tau}\sigma_{ec}\left|\nabla V\right|^2 dt \quad \text{(2-11)}$$

In electrical motors, a suitable cooling system is required to mitigate the inside thermal stresses. Fig. 2-6 illustrates a typical cooling system based on a water flow in a helical duct in rotating machines [37]. This system directly contacts the stator laminations, and hence allows the cooling water to receive heat generated by iron losses in the stator laminations and Joule losses in the stator conductor bars effectively. Of course, the heat generated in SGSs on stator conductor bars can partially be transferred to the cooling water flow by conduction through the inside part of the CAT and stator laminations. Besides, air convection caused by fans installed on the rotor shaft can significantly dispatch the heat in the motors.

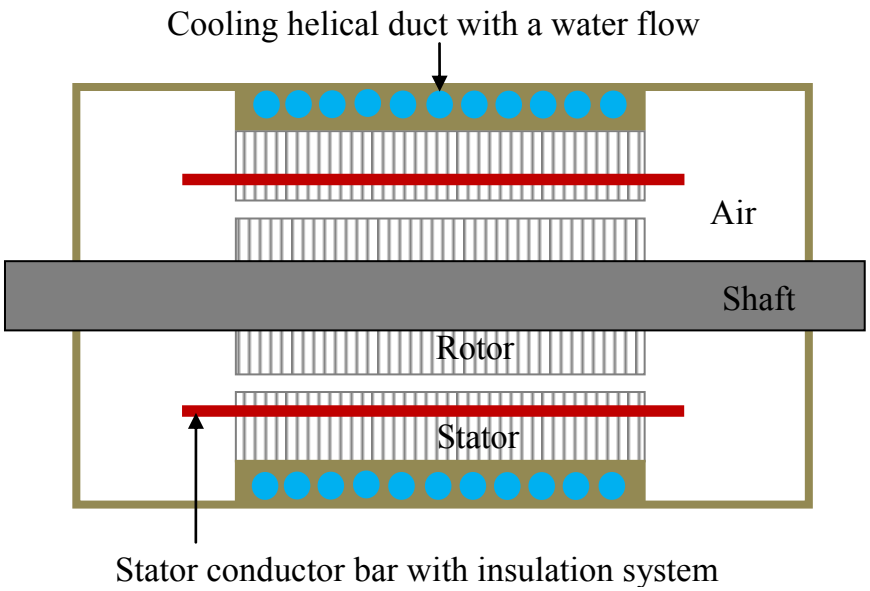

Fig. 2-6: *A typical cooling system for high power motors* [37].

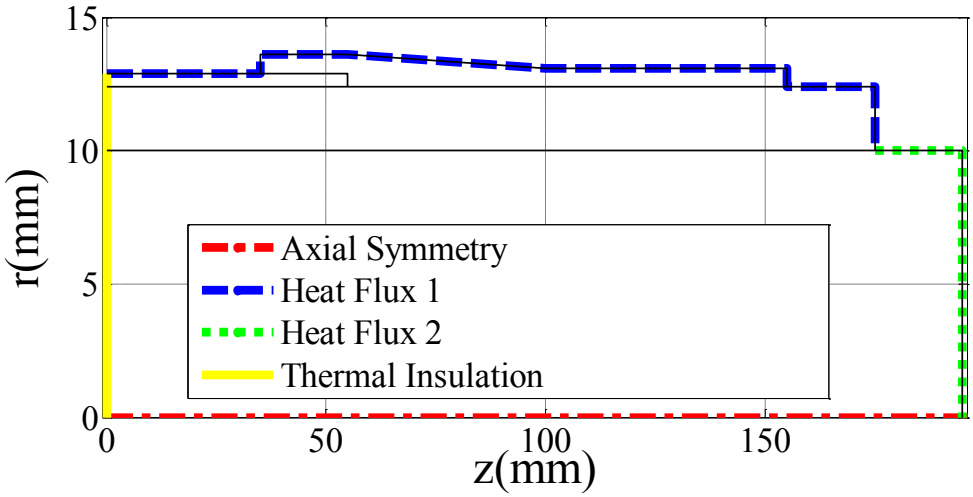

Fig. 2-7: *Boundary conditions used in the heat transfer analysis model.*

Obviously, the above cooling mechanisms are necessary for the selection of conditions for the boundaries truncating the analyzed space domain of the SGS. Fig. 2-7 outlines the boundary conditions used in this thermal analysis.

On the boundary between the considered SGS and the left part of the conductor bar inside the stator slot, the yellow line in Fig. 2-7, there is a heat

flow from the SGS towards the cooling system. However, in this analysis, the thermal behavior of the SGS is studied in a serious condition without any heat transfer at this boundary. Hence, the thermal insulation condition based on the equation (2-12) is chosen at this boundary.

$$-\vec{n}\cdot\left(-k\nabla T\right)=0 \quad \text{(2-12)}$$

On the surfaces separating the SGS and the air, the blue and green lines in Fig. 2-7, the air convection and the radiation heat transfer mechanisms occupy, thus the heat flux conditions based on the equation (2-13) are suitable choices. In the equations (2-12) and (2-13), $\vec{n}$, h (W/(m^2·K)), T_{ext} (K), ε_{ra} are the unit normal vector, the heat transfer coefficient, the external temperature, and the emissivity coefficient, respectively, and σ_{SB} = 5.6703×10^{-8} W/(m^{2}K^4) is the Stefan-Boltzmann constant. The first term on the right side of the heat flux equation expresses the convective heat transfer process at the surfaces between the solid materials and the surrounding air. The heat transfer coefficient of this process is required to be measured to get the exact value because it is highly dependent on the complicated structure of end-winding insulation systems and surrounding air flows [38]. For example, it is recorded within the range from 14 to 24 W/(m^2·K) [38]. Hence, for the general calculation in this case, the heat flux boundaries in this model is set with the convective heat transfer coefficient of 20 W/(m^2·K). Meanwhile, the second term on the right side of equation (2-13) describes the radiation heat transfer process from the surfaces of the SGS. Based on the data in [39], the emissivity coefficient of the heat flux 1 on the surfaces of CAT, SGT and main insulation is assumed to be 0.9 while the one of the heat flux 2 on the surfaces of copper conductor is 0.03. In addition, both the initial and the external temperatures are assumed to be 30 ^{o}C.

$$-\vec{n}\cdot(-k\nabla T)=h(T_{ext}-T)+\varepsilon_{ra}\sigma_{SB}\left(T_{ext}^4-T^4\right) \quad \text{(2-13)}$$

In FEM based package like COMSOL, the mesh profile is very important. As displayed in Fig. 2-8, the mesh used in the two analysis models is set up with high thickness in areas of thin structures as CAT and SCT. This advanced feature of FEM allows the models to enhance the accuracy in computation while keeping the memory cost in a reasonable limitation.

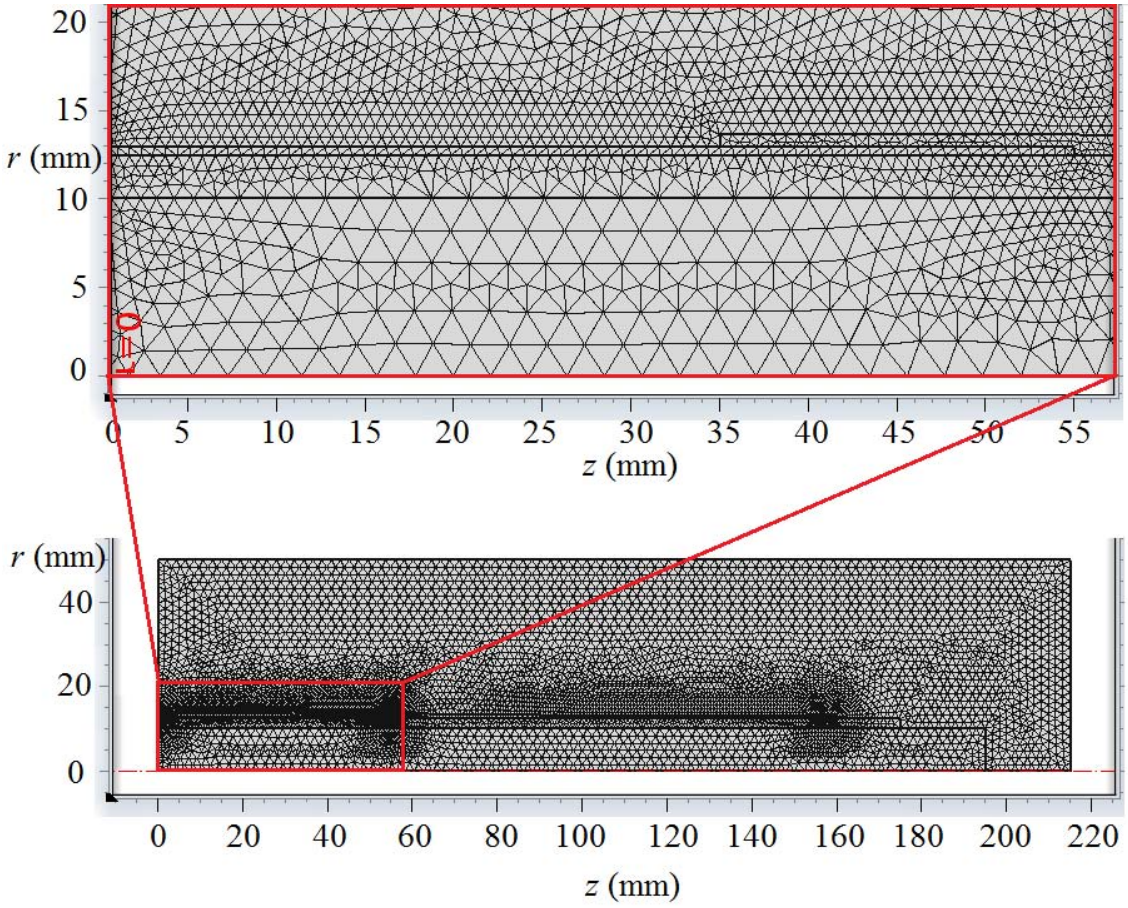

Fig. 2-8: *The mesh profile of the SGS used in the two analysis models.*

2.3 Series Connected H-Bridge voltage source converter model

Multilevel converters are used more and more commonly to overcome the voltage limit capability of semiconductor devices [40]. There are three typical standard products for industrial medium voltage drives [40]: 1) the 3-level neutral point clamed voltage source converter (NPC VSC); 2) the 4-level flying capacitor (FC) VSC; and 3) the Series Connected H-Bridge (SCHB) VSC. Besides, a hybrid topology can be achieved based on the cooperation between the SCHB and NPC structures.

From the technical and the economic analyses based on the comparison of NPC, FC and SCHB topologies [41], the multi-level SCHB scheme whose block diagram is displayed in Fig. 2-9 is the suitable choice for high power rating converters. Hence, this topology using 5-level (5L) and 11-level (11L) structures is chosen to provide 11 kV (line-to-line) PWM voltage waveforms for the electric field and the heat transfer analyses in the previous parts. The phase shifted sine pulse width modulation strategy is applied to generate the control signals for these two converters. Calculations and simulations for this converter type are mainly based on the procedure provided by Islam M. R. et al. in Matlab/Simulink environment [41]. The fundamental data of these inverters are summarized in Table 2-3.

Table 2-3: *Basic data of the SCHB VSCs.*

	Output voltage (line-to-line)	**Nominal DC-link voltage**	**Carrier frequency**	**Output frequency**
Values	11 kV_{RMS}	16.179 kV	750 Hz	50 Hz

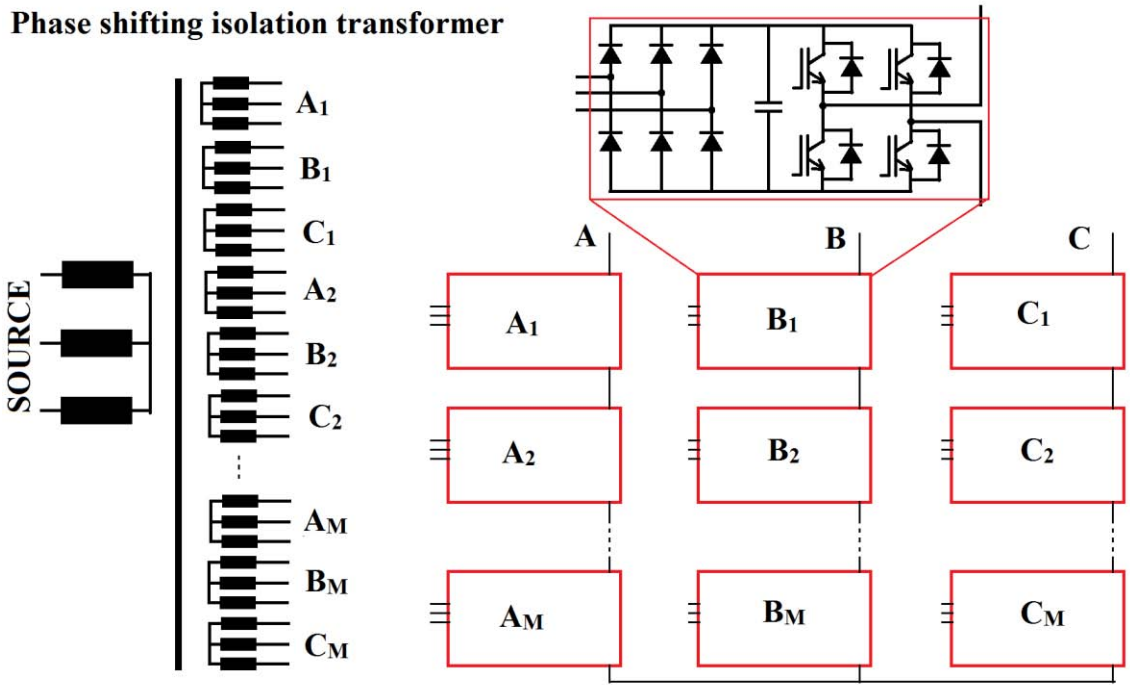

Fig. 2-9: *Typical topology of a (2M+1)-level SCHB VSC* [1, 42].

The model of the SCHB VSC used in this work is provided by Mr. Le Dinh Khoa who is studying at the Doctor course of Waseda University.

2. 4 Mathematical model for PWM surge transmission in ASD networks

In a standard application of ASD illustrated in Fig. 1-1, the output PWM voltage of the converter is fed to the motor through a cable system. The voltage overshoot is unavoidable at the motor terminal because of the impedance mismatch between the cable and the motor [27]. Hence, for assessment of the stress grading performance, the PWM voltage at the motor side has to be predicted. To handle this problem, Electromagnetic Transient Program (EMTP) is the most popular way [43-44] while the classical Lattice diagram has been applied for a very long time [45]. Recently, finite difference method was used to analyze an actual structure of an ASD application [27]. Besides, a mathematical

model derived from the telegrapher's difference equations was proposed in [45]. This model is validated to be not only precise but also quite simple [45]. All the needed data for this technique are the output voltage and surge impedance of the converter; the length, wave travelling velocity and surge impedance of the connecting cable; and the surge impedance of the motor. Hence, this model is employed and modified to predict the PWM voltage waveforms arriving at the end-winding insulation systems.

Before going into this model, it is necessary to introduce the surge impedances of cable Z_C (Ω) and motor Z_M (Ω) which are calculated by equation (2-14) and (2-15), respectively. In these equations, L_C (H/m) and C_C (F/m) are the inductance and the capacitance per unit length of the cable; L_M (H) is the inductance of the motor and C_M (F) is the capacitance of the motor stator winding. Besides, during the switching process, an inverter can be considered as a serial network of dc bus capacitor, stray inductance and resistance; hence, it has a small intrinsic surge impedance *Zs* (Ω) [45]. In general, the motor surge impedance is supposed to be much higher than the one of the cable [45].

$$Z_C = \sqrt{\frac{L_C}{C_C}} \quad \text{(2-14)}$$

$$Z_M = \sqrt{\frac{L_M}{C_M}} \quad \text{(2-15)}$$

The key equation proposed by S. Amarir and K. Al-Haddad [45] to calculate the voltage at the motor side V_M based on the one at the inverter side V_S are as follows

$$V_M(t) = \frac{Z_C}{Z_S + Z_C} \sum_{n=0}^{\infty} \left\{ \left(K_M^n K_S^n + K_M^{n+1} K_S^n \right) \cdot V_S\left[t - (2n+1)\tau\right] \cdot u_S\left[t - (2n+1)\tau\right] \right\} \quad \text{(2-16)}$$

In this equation, K_M and K_S are the reflection constants due to the impedance mismatch at the interfaces of cable-motor and of cable-inverter, respectively. These constants can be calculated by equations (2-17) and (2-18). Besides, τ (s) is the travelling time of the PWM wave from the inverter to the motor and is calculated based on the cable length *l* (m) and the travelling velocity of wave through the cable *v* (m/s) as in equation (2-19). Another symbol in equation (2-16) is the unit step function $u_S(t)$.

$$K_M = \frac{Z_M - Z_C}{Z_M + Z_C} \quad \text{(2-17)}$$

$$K_S = \frac{Z_S - Z_C}{Z_S + Z_C} \quad \text{(2-18)}$$

$$\tau = \frac{l}{v} \quad \text{(2-19)}$$

In [45], the received voltage at the motor is calculated using the equation (2-16) with the algorithm for Matlab/Simulink in Fig. 2-10. In this computation, $V_n(t)$ ($n=0, 1, 2, 3, \ldots, N$) is a term in a limited series, and is calculated as follows

$$V_n(t) = \frac{Z_C}{Z_S + Z_C} \left\{ \left(K_M^n K_S^n + K_M^{n+1} K_S^n \right) \cdot V_S\left[t - (2n+1)\tau\right] \cdot u_S\left[t - (2n+1)\tau\right] \right\} \quad \text{(2-20)}$$

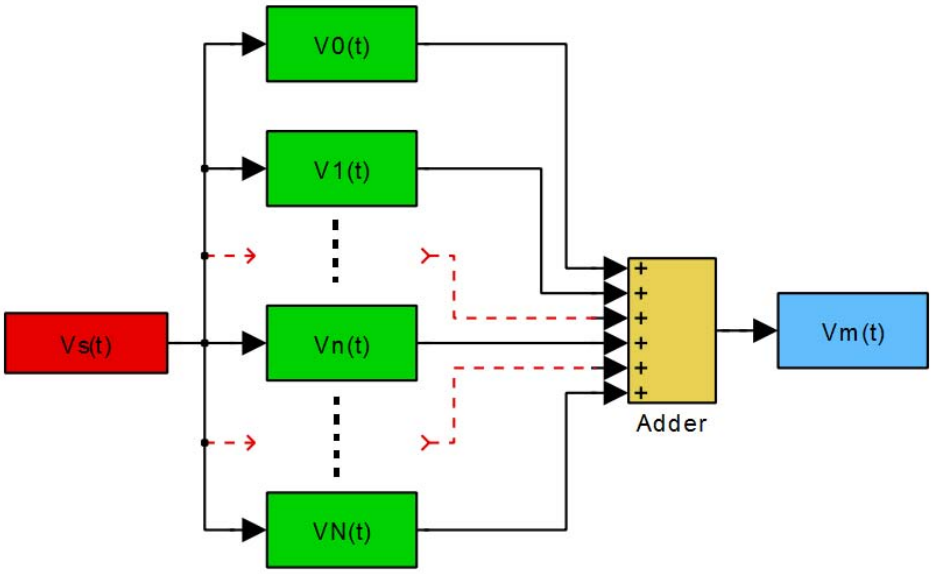

Fig. 2-10: *Computation algorithm of V_M for Matlab/Simulink used in* [45].

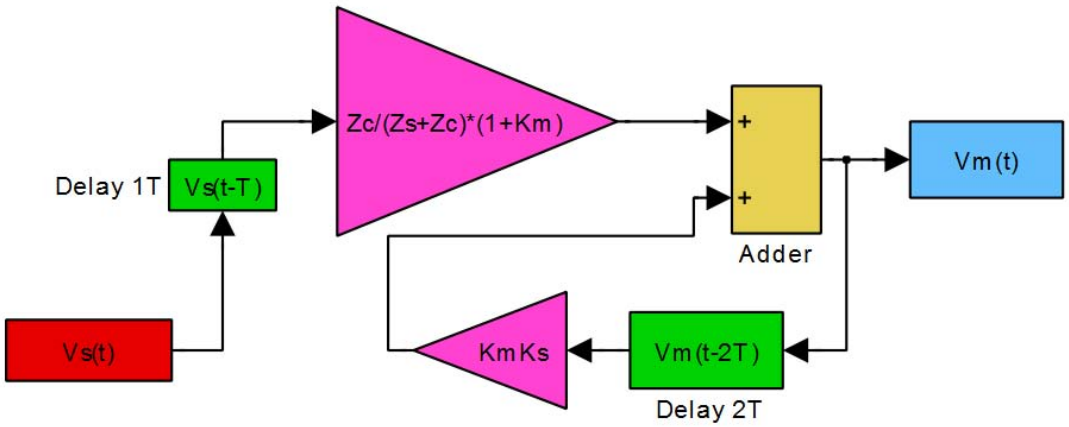

Fig. 2-11: *Improved computation algorithm of V_M for Matlab/Simulink in this work.*

In this work, derived from the equation (2-16), a close-loop formula of the received voltage at the motor terminal is proposed in the equation (2-21). Hence, the computation algorithm for Matlab/Simulink can be improved as in Fig. 2-11.

$$V_M(t) = \frac{Z_C}{Z_S + Z_C}(1 + K_M K_S)V_S(t-\tau) + K_M K_S V_M(t-2\tau) \quad \text{..... (2-21)}$$

Chapter 3

RESULTS

3.1 Frequency response of the stress grading system

This section focuses on analyzing the frequency response of the SGS under the range from 50 Hz to 5 MHz. For this investigation, 5.5 kV_{RMS} sinusoidal sources are applied as the electric potential boundary conditions in the electric field analysis model.

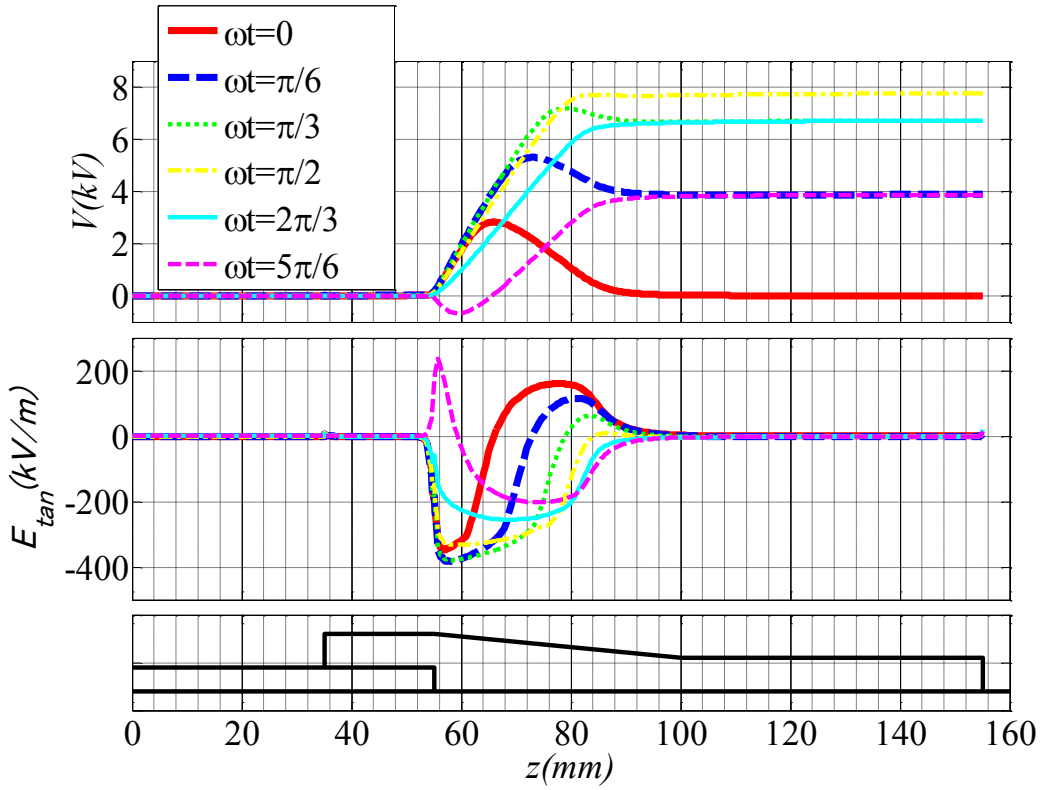

Fig. 3-1: *Electric potential and tangential electric field stress on the surfaces of the SGS in case of 50* Hz *sinusoidal voltage source.*

Firstly, it is necessary to start this analysis with the industrial frequency of 50 Hz. Fig. 3-1 displays the distributions of the electric potential and the surface tangential electric stress on the SGS. For the tangential electric field component, the conventional direction is chosen from the low to the high value of the z-axis. In this case, the CAT is kept at zero potential and does not suffer from the electric field stress. Besides, the maximum tangential electric field stress on the SGS is 386.3 kV/m, and this value is much lower than the PD threshold of 642 kV/m recorded in clean conditions under the industrial frequency sources [46]. On the other hand, the dissipated power is mainly located inside the SCT near the CAT and heats up this area as illustrated in Fig. 3-2. These results demonstrate that for the 50Hz sinusoidal voltage source, the SGS is in an effectively working condition and PD is prevented successfully.

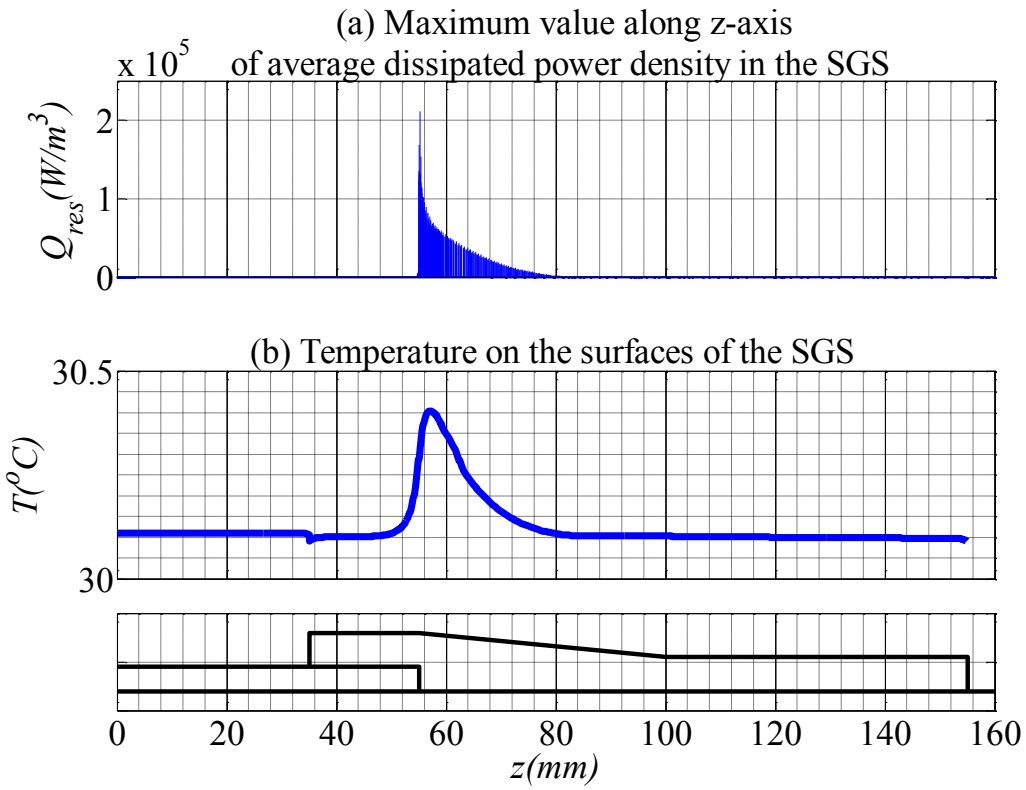

Fig. 3-2: *Maximum value along z-axis of average dissipated power density in the SGS and maximum temperature on the surfaces of the SGS in case of 50* Hz *sinusoidal voltage source.*

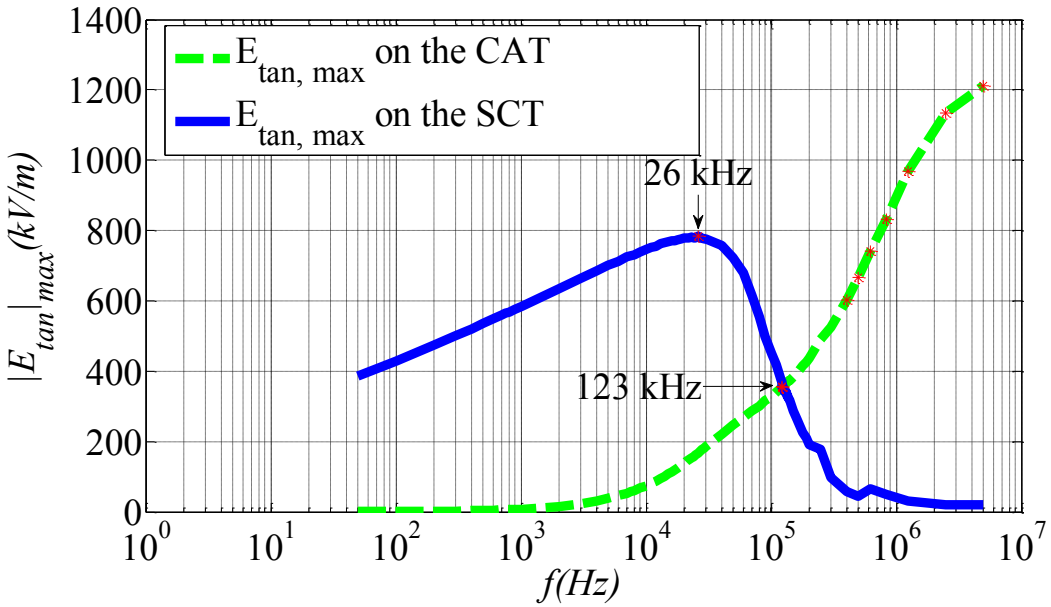

Fig. 3-3: *Maximum tangential electric field stress on the surfaces of the CAT and the SCT in case of sinusoidal voltage sources with the frequency from 50* Hz *to 5* MHz.

Secondly, this analysis is conducted in much higher frequency conditions to investigate the working ability of the SGS which is supposed to go down with the increase of the frequency [17-18]. This trend is validated through the changes of the maximum tangential electric field stress at the stator slot exit (z = 0 mm) on the CAT and on the SCT in the range of frequency from 50 Hz to 5 MHz as in Fig. 3-3. The tangential electric field stress on the surface of the CAT increases with the growth of frequency while this stress on the surfaces of the SCT changes in two different stages. In the first stage from 50 Hz, it increases as a logarithmic function of frequency up to the maximum value of 784 kV/m at 26 kHz. After that it goes into the second period with the reduction. From the frequency of 123 kHz, the tangential electric field stress on the CAT becomes much higher than that on the SCT. An important finding is that the effective area of the SCT decreases with the rise of frequency. This trend is validated by observing the maximum tangential electric field stress distribution on the SGS in Fig. 3-4.

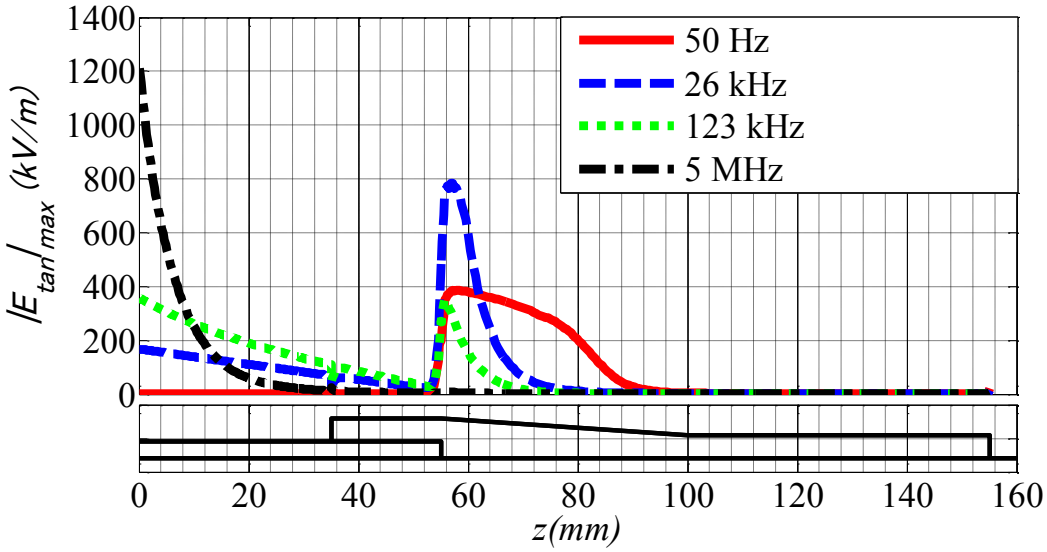

Fig. 3-4: *Maximum tangential electric field stress on the surfaces of the SGS in the four cases 50* Hz*, 26* kHz*, 123* kHz *and 5* MHz *sinusoidal voltages.*

Another problem is that the dissipated power loss in the SGS becomes higher in high frequency conditions, especially at the area in the CAT near the stator slot exit. As a result, the temperature in the SGS increases rapidly. The maximum values of this parameter on the surfaces of the CAT and the SCT in the range of frequency from 50 Hz to 20 kHz are displayed in Fig. 3-5 as an evidence of the devolution in the working ability of the SGS. The higher the frequency is, the lower the effect of the SGS becomes.

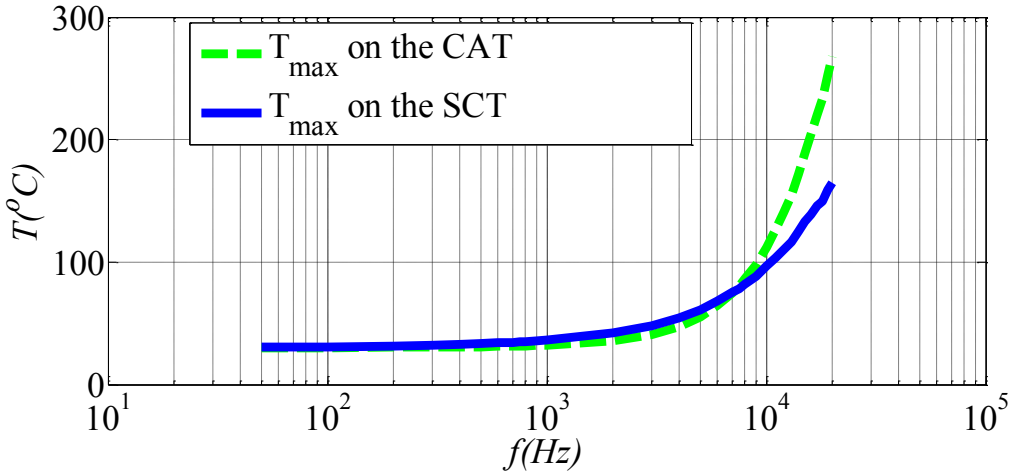

Fig. 3-5: *Maximum temperature on the surfaces of the CAT and the SCT in case of sinusoidal voltage sources with the frequency from 50* Hz *to 20* kHz*.*

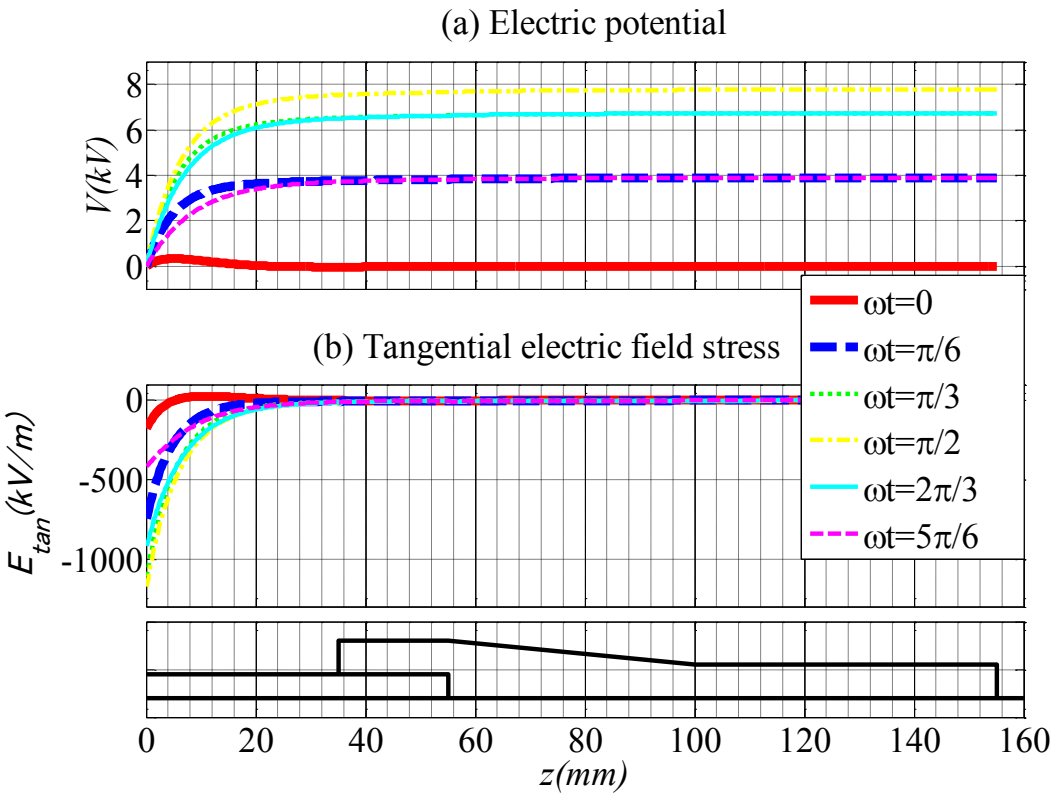

Fig. 3-6: *Electric potential and tangential electric field stress on the surfaces of the SGS in case of 5* MHz *sinusoidal voltage source.*

A typical illustration for the failure of the SGS under very high frequency conditions is considered in Fig. 3-6 when the frequency is 5 MHz. In this case, the stress relieving effect of the SGT is almost disappeared and hence, the tangential electric field stress is highly located on the CAT at the stator slot exit. In contrast to the 50 Hz source, PD can strongly develop at this position due to the high electric field stress in this condition.

3.2 Operation analysis of the stress grading system under PWM voltage sources

3.2.1 Output voltages of the SCHB VSCs

For a comparison, the 5L-SCHB and the 11L-SCHB VSCs are controlled to provide the same phase-to-phase output voltage RMS value of 9 kV with the modulation indices of 0.872 and 0.903, respectively. The phase-to-ground of the

output voltages from the two inverters are displayed in Fig. 3-7. The two voltage waveforms are then analyzed using Fourier transformation to get the harmonic spectra shown in Fig. 3-8. The effective frequencies of these inverters which are 3 kHz and 7.5 kHz of the 5L and the 11L SCHB VSC, respectively can be predicted using equation (3-1) [42]. In this equation, M is the number of H-Bridge in the inverters (2 and 5 for the 5L and 11L inverters, respectively), and f_{ca} is the frequency of the triangular carrier wave (750 Hz for these two inverters). The fundamental harmonic (FH) and the total harmonic distortion (THD) of the phase voltages in these two cases are presented in Table 3-1. These results provide a clear view of the harmonic spectrum in the output of the two SCHB VSCs.

$$f_{eff} = 2Mf_{ca} \quad \text{.....(3-1)}$$

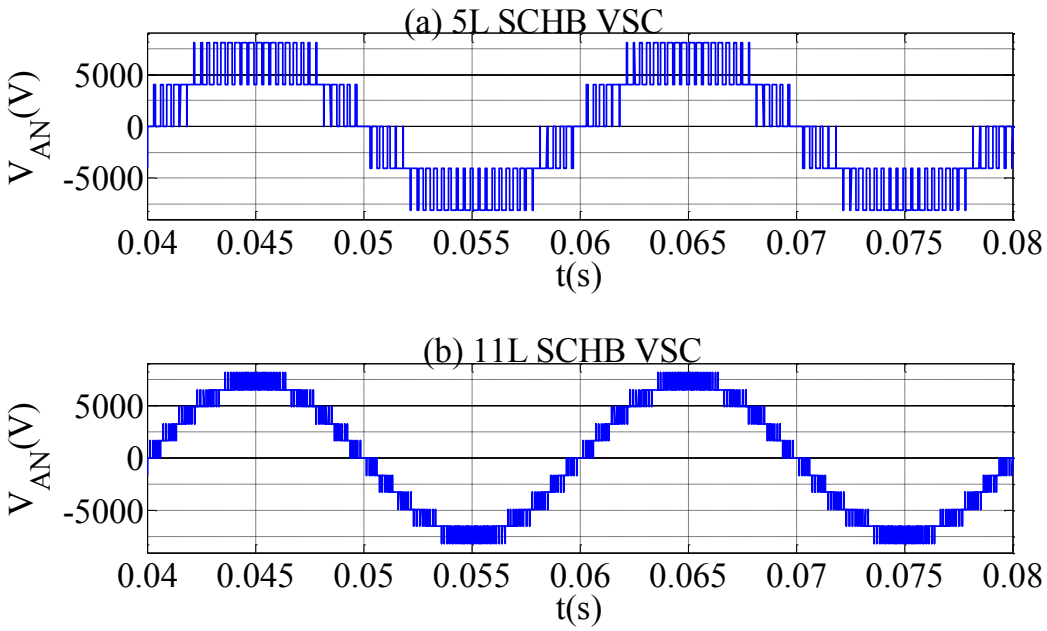

Fig. 3-7: *Output phase-to-ground voltages of the 5L SCHB and 11L SCHB VSCs.*

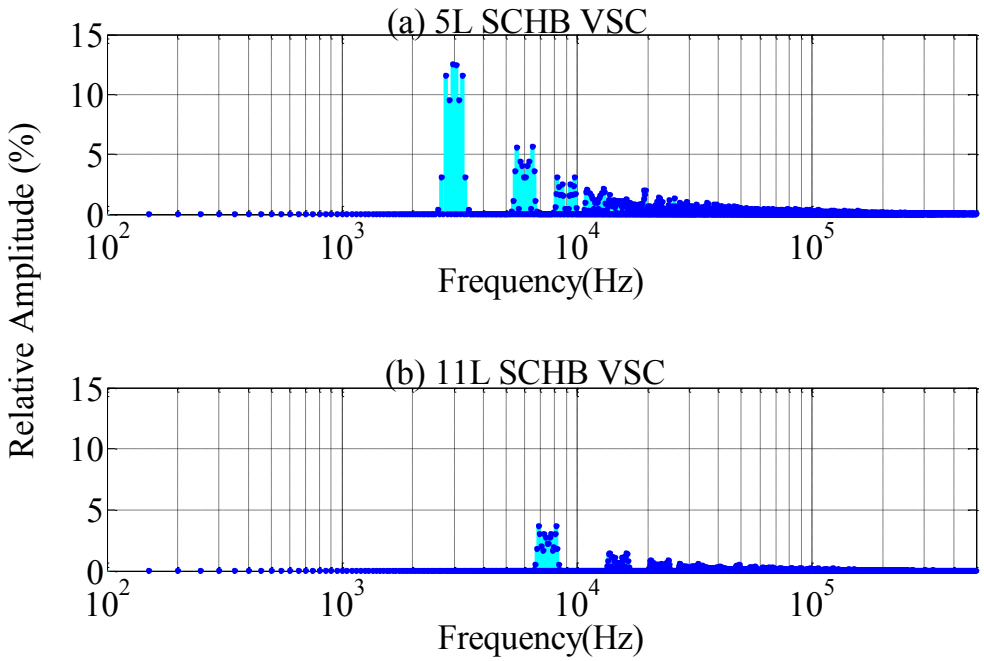

Fig. 3-8: *Harmonic spectra in the phase-to-ground voltages of the 5L and the11L SCHB VSCs.*

Table 3-1: *Fundamental harmonic and THD of the phase voltage provided by the 5L and the 11L SCHB VSCs.*

5L SCHB VSC		**11L SCHB VSC**	
FH (kV)	**THD (%)**	**FH (kV)**	**THD (%)**
7.055	34.93	7.304	13.10

An important parameter of the PWM voltages is the rise time. The range of this parameter in commercial inverters is from 50 ns to 2000 ns [2]. In this subsection, the rise time of 1000 ns is chosen for analysis. Besides, the overshooting phenomenon due to impedance mismatch between the connecting cable and the motor is ignored, and hence, the PWM voltage at the motor terminal is assumed to be the same as the one at the inverter side.

3.2.2 Electric field analysis

The phase-to-ground voltages of the 5L and the 11L SCHBVSCs are inputted into the electric field analysis model as the electric potential boundary conditions. For the voltage rise time of 1 μs, the sampling increment of 0.05 μs is chosen for the time domain analysis. The step-running strategy in COMSOL is conducted to overcome the limitation of memory cost. In order to analyze the electric field in the SGS in a half fundamental duty cycle duration of 10 ms, 500 analysis steps of 20 μs are conducted.

Fig. 3-9 presents the maximum tangential electric field on the SGS in the three cases of 5L, 11L SCHB VSCs and sinusoidal voltage source. Two special positions which have to be paid attention are the stator slot exit on the CAT (at z = 0 mm) and the one on the SCT near the end of the CAT (at z = 56.9 mm). The tangential electric field at these two points during the second-half fundamental duty cycle is recorded in Fig. 3-10. For more details, the amplitude, appearance time and location of the maximum tangential electric stress on the SGS are displayed in Table 3-2.

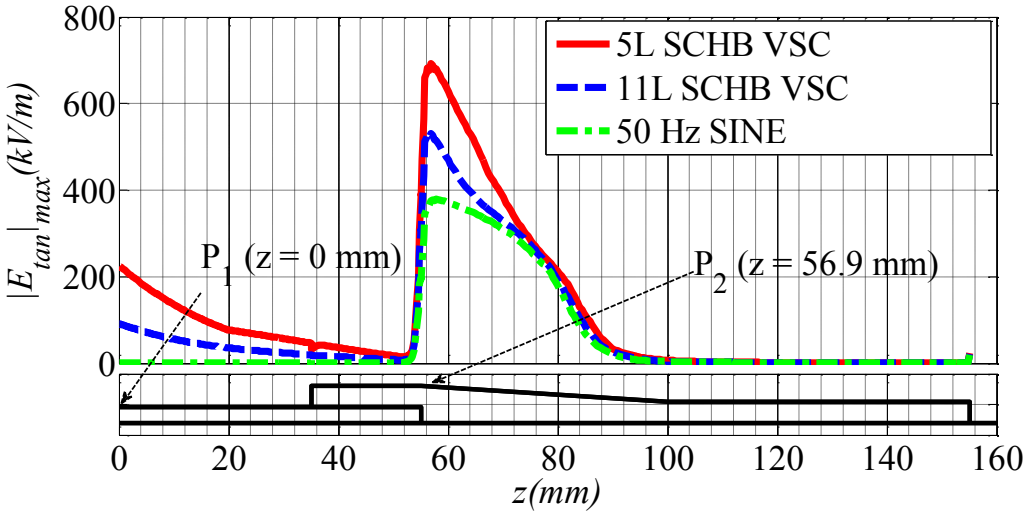

Fig. 3-9: *Maximum tangential electric field stress on the surfaces of the SGS in the three cases of 5L, 11L SCHB VSCs and 9 kV_{RMS} (phase-to-phase) sinusoidal voltage source.*

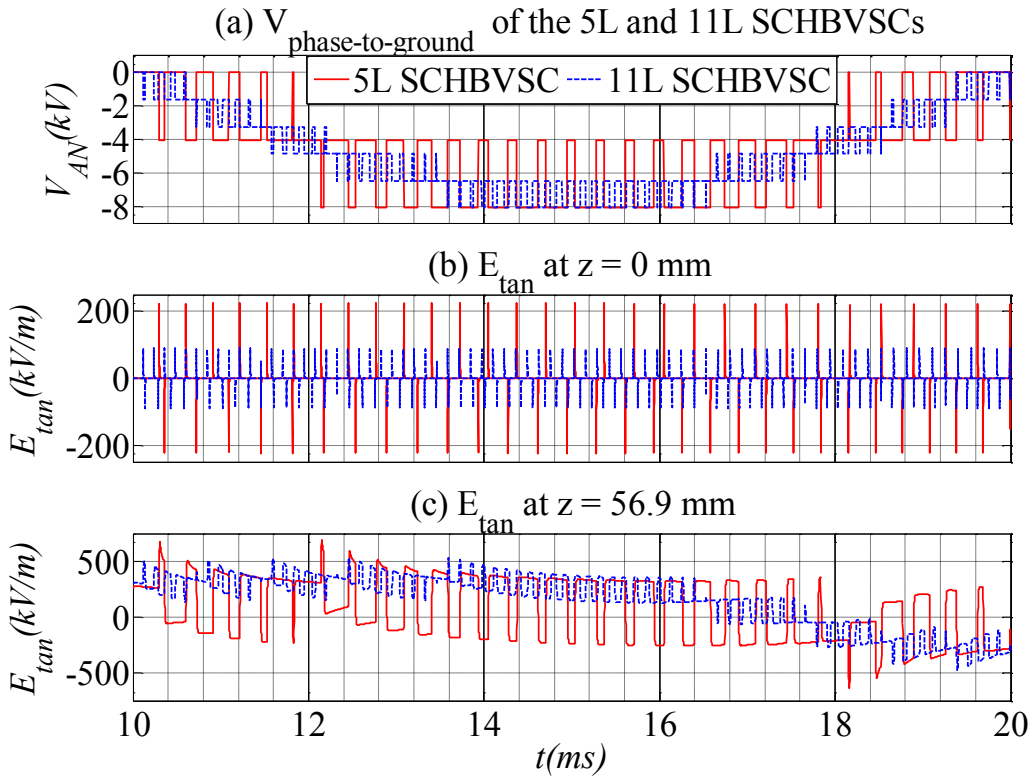

Fig. 3-10: *Tangential electric field on the surfaces of the SGS at the two points (z = 0 mm and z = 56.9 mm) in the two cases of 5L and 11L SCHB VSCs during the interval from 10 ms to 20 ms.*

Table 3-2: *Amplitude, appearance time and location of maximum tangential electric field stress on the surface of the SGS in the three cases of 5L, 11L SCHB VSCs and 9 kV_{RMS} (phase-to-phase) sinusoidal voltage source.*

	5L SCHB VSC	**11L SCHB VSC**	**SINE**
$\|E_{tan}\|_{max}$(kV/m)	692.6	530.9	378.7
t(ms)	12.150	12.461	12.333
z(mm)	56.9	56.9	57.8

Based on the time when the highest tangential electric stress appears on the SGS in Table 3-2, the tangential electric stresses at the two special positions are displayed in Fig. 3-11 from 12.14 ms to 12.18 ms for the 5L inverter and in Fig. 3-12from 12.445 ms to 12.475 ms for the 11L inverter .

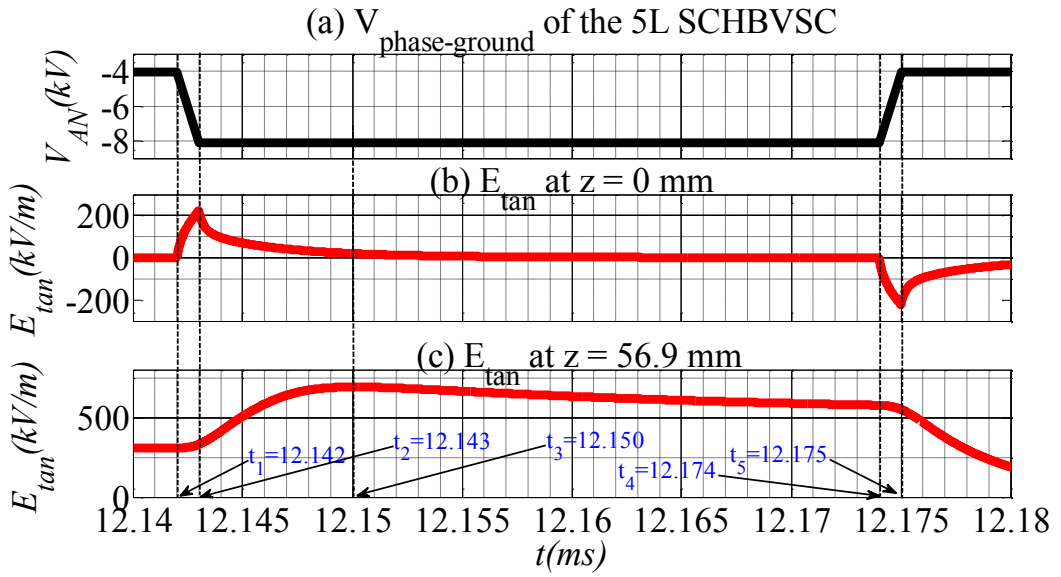

Fig. 3-11: *Tangential electric field on the surfaces of the SGS at the two points (z = 0 mm and z = 56.9 mm) in the case of 5L SCHB VSC during the interval from 12.14 ms to 12.18 ms.*

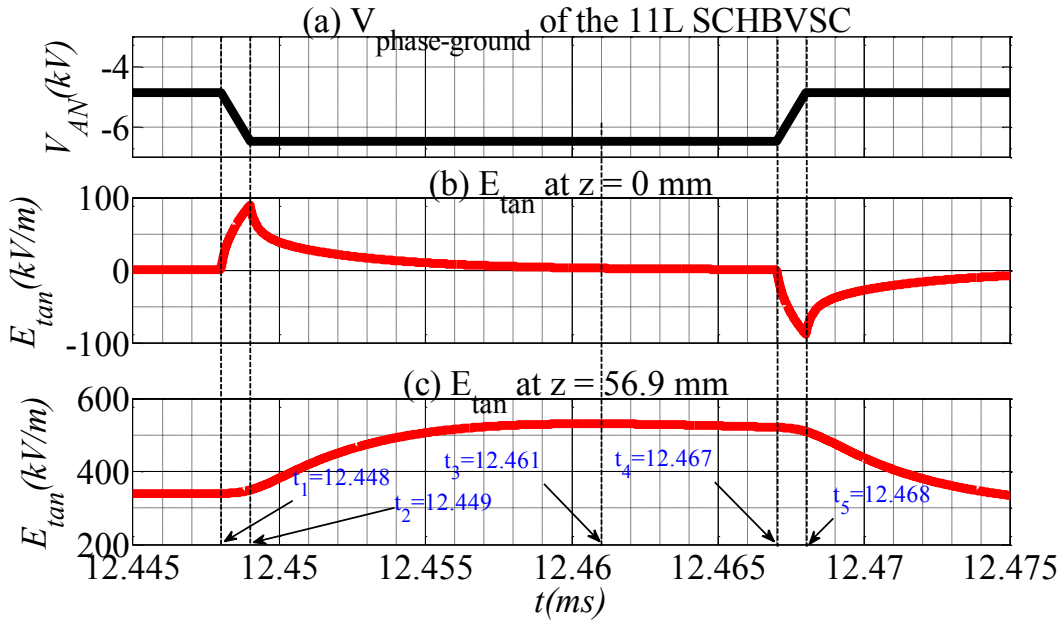

Fig. 3-12: *Tangential electric field on the surfaces of the SGS at the two points (z = 0 mm and z = 56.9 mm) in the case of 11L SCHB VSC during the interval from 12.445 ms to 12.475 ms.*

Table 3-3: *Important differences of tangential electric field stress at the two special positions on the SGS in the cases of 5L and the 11L SCHB VSCs.*

	Feature	***z* = 0 mm (on the CAT)**	**z = 56.9 mm (on the SGS)**
1	Response speed	Immediately changes with the voltage sources	Have a delay in change with the voltage sources
2	Existing time	Very short (8 µs for 5L inverter and 13 µs for 11L one) from the change of the voltage sources	Much longer than the one on the CAT.
3	Impact factors of the voltage sources	Rise rate (*dV/dt*)	Rise rate (*dV/dt*), effective frequency, fundamental frequency

Derived from the results in Fig. 3-10, Fig. 3-11 and Fig. 3-12, some important differences of tangential electric field stress at the two special positions can be summarized in Table 3-3.

It is observed in the both cases of the inverters that the highest tangential electric field locates on the surface of the SCT at the transition area with the CAT. The inception field strength of PD is 600 kV/m defined in [2], but it is also recorded as low as 450 kV/m under fast impulse conditions [17]. Hence, PD can develop at the surface area of the SCT for the 5L inverter and it can be prevented for the 11L one. To give a more detailed view of the SGS operation, the distribution of electric potential and tangential electric field stress on the surfaces of the SGS during the interval from 12.14 ms to 12.18 ms for the 5L VSC and from 12.445 ms to 12.475 ms for the 11L one can be observed in Fig. 3-13 and Fig. 3-14, respectively.

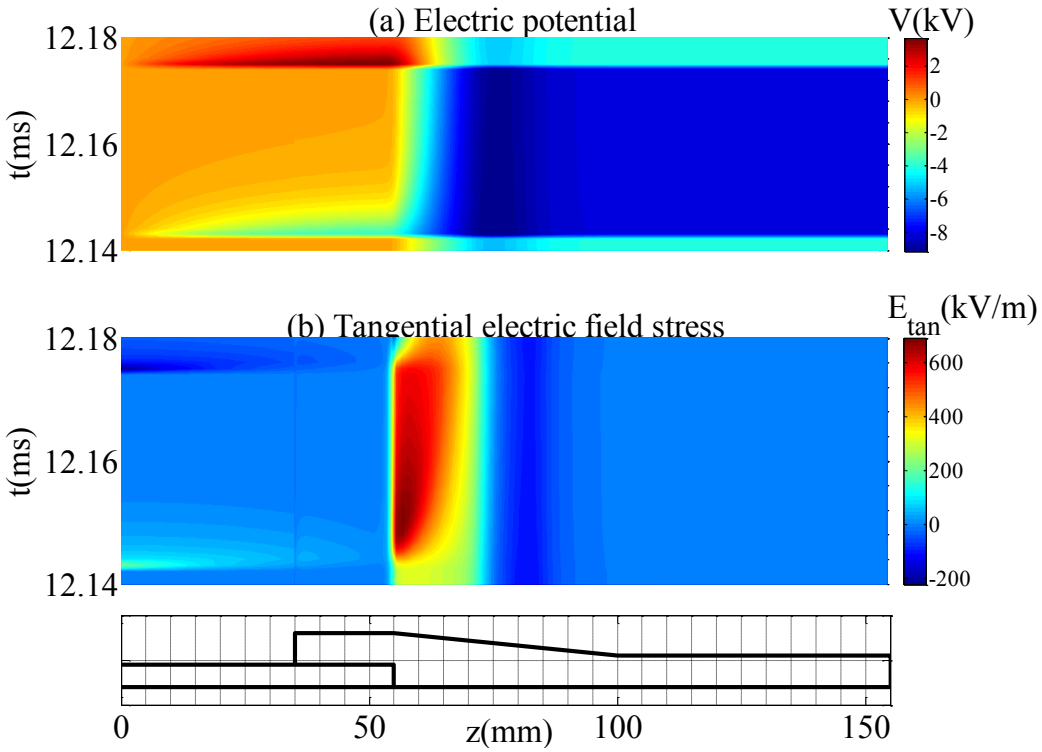

Fig. 3-13: *Distribution of electric potential and tangential electric field on the surfaces of the SGS during the interval from 12.14 ms to12.18 ms in the case of 5L SCHB VSC.*

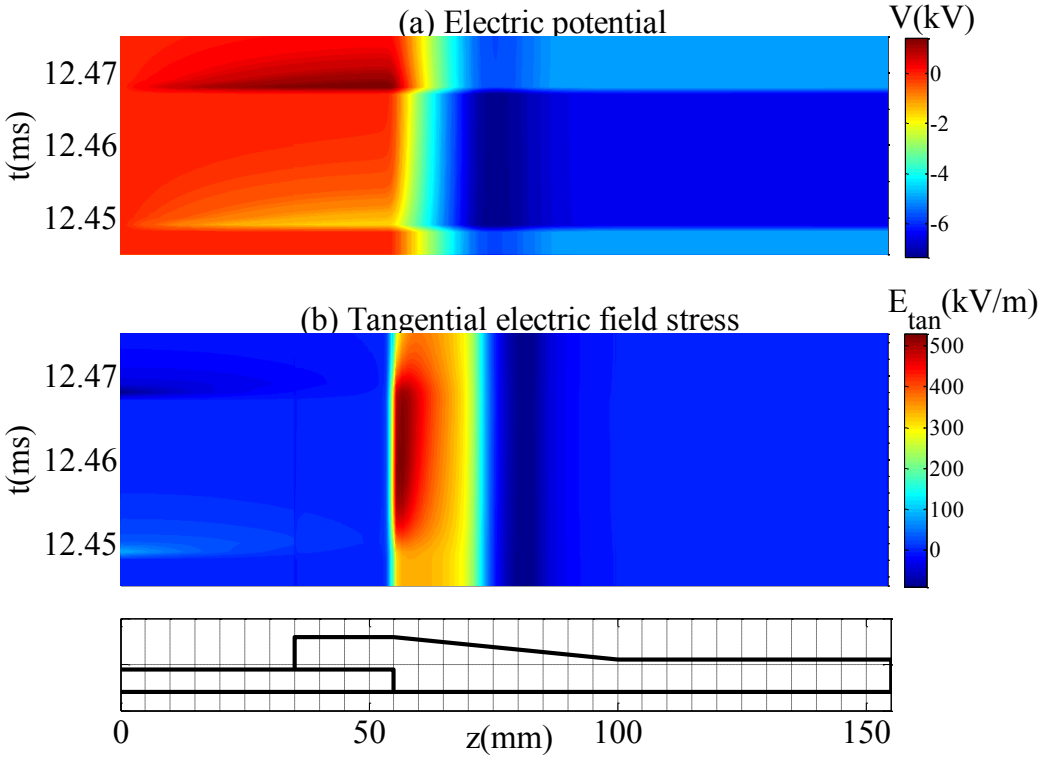

Fig. 3-14: *Distribution of electric potential and tangential electric field on the surfaces of the SGS during the interval from 12.445 ms to12.475 ms in the case of 11L SCHB VSC.*

Based on this electric field analysis, the average dissipated power density inside the SGS during a haft duty cycle is calculated and considered as the constant heat source density in the following heat transfer analysis model.

3.2.3 Heat transfer analysis

The maximum values along z-axis of the average dissipated power density in the cases of two inverters are presented in Fig. 3-15. This loss density is observed to concentrate highest at the region near the stator slot exit (at z = 0 mm) in the CAT and at the region near the end of the CAT (at z = 55 mm) in the SCT. The temperature distributions on the surfaces of the SGS in the two inverter cases are compared with the one in the case of sinusoidal voltage source and displayed in Fig. 3-16. The hottest point is at the stator slot exit (z = 0 mm) on the CAT for the two SCHB VSCs. On the other hand, the highest temperature near the end of the CAT on the SGT is observed for the sinusoidal voltage source (z = 57.0 mm). The temperature profiles in the SGS are summarized in Table 3-4.

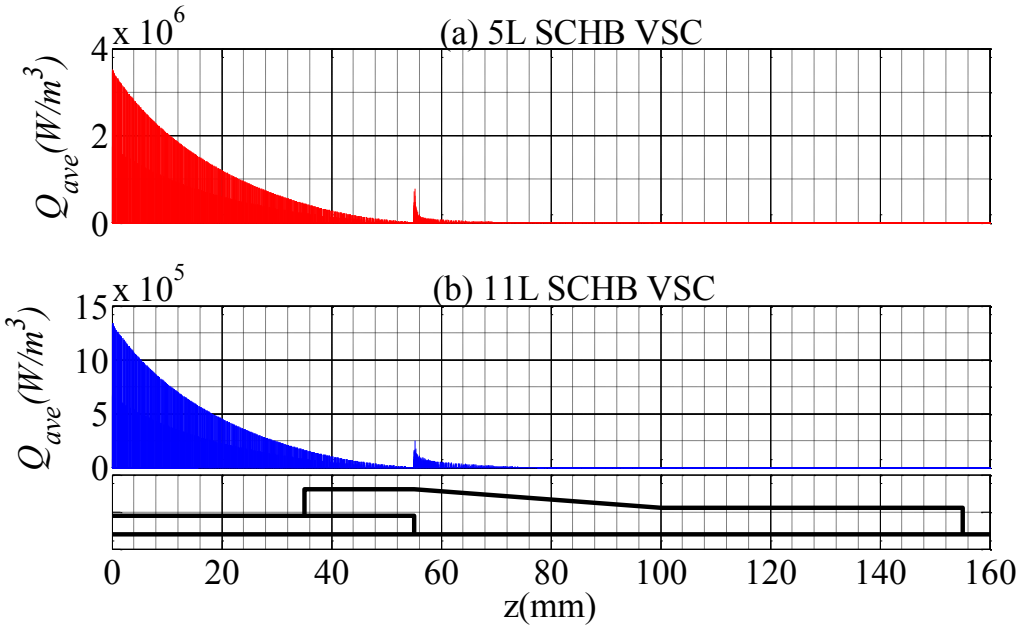

Fig. 3-15: *Maximum value along z-axis of average dissipated power density in the SGS in the cases of 5L and 11L SCHB VSCs.*

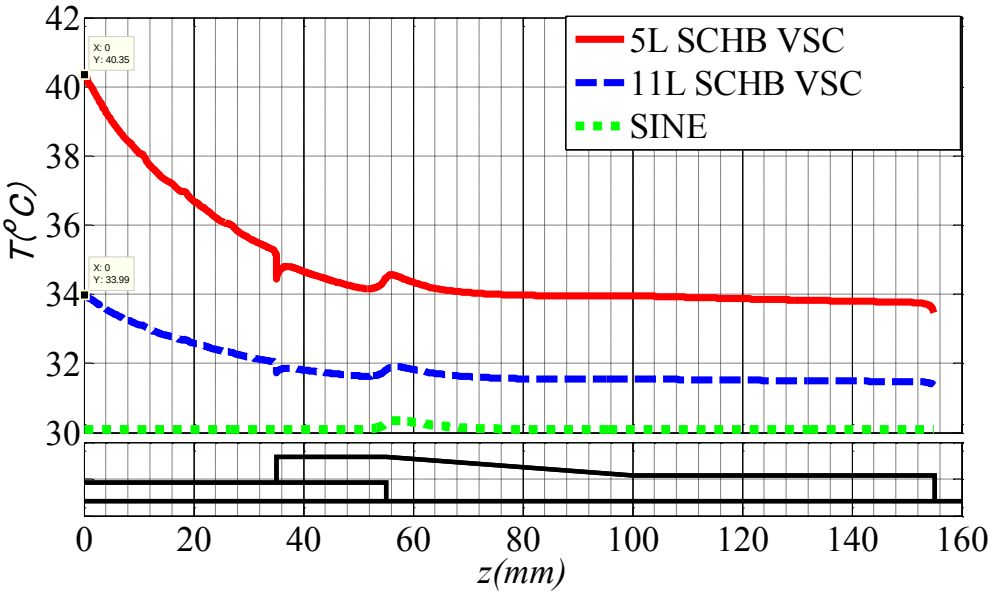

Fig. 3-16: *Temperature distribution on the surfaces of the SGS in the three cases of 11L, 5L SCHB VSCs and sinusoidal voltage source after 30 hours.*

Table 3-4: *Important data of temperature distribution in the SGS from the heat transfer analyses.*

	Highest temperature rise				
	Inside the SGS			On the surfaces of the SGS	
	Position (mm)		Value (°C)	Position (mm)	Value (°C)
	r	*z*	*ΔT*	*z*	*ΔT*
5L SCHB VSC	12.7	0	10.42	0	10.35
11L SCHB VSC	12.7	0	4.02	0	3.99
$9kV_{RMS}$ 50 Hz Sine	13.2	57.0	0.36	57.0	0.36

From these above analyses, the reason why the temperature at the area near the stator slot exit on the SG system becomes high under PWM voltage

source conditions is now clear. This is basically the result of the high density of the dissipated power density inside the CAT area near this location in a short existing duration from the rising time of the impulses of the PWM voltages.

3.3 Investigation of the effect of overshot voltage due to impedance mismatch between cable and motor

In this section, the effect of overshot voltage on the operation of the SGS is studied for the case of 11L SCHB VSC. Firstly, a fundamental case is chosen for the operation analysis of the SGS under the 11L inverter voltage with the sampling increment of 0.05 μs. From this analysis, a simplified voltage waveform is proposed to conduct the electric field analysis with sampling time of 2.5 ns for some typical cases with shorter rise times and shorter cables.

3.3.1 Fundamental case

The simulation parameters of the inverter, the cable and the motor for surge-travelling analyzing used in this case are summarized in Table 3-5. It is noted that the length and the travelling velocity of the cable are chosen so that the travelling time between the two sides of the cable is equal to the rise time of 1μs..

Table 3-5: *Surge characteristics of the inverter, the cable and the motor in the fundamental case.*

	Impedance Z (Ω)	**Length *l* (m)**	**Travelling velocity *v* (m/μs)**	**Rise time t_r (μs)**
Inverter	0.1	x	x	1
Cable	25	150	150	x
Motor	100	x	x	x

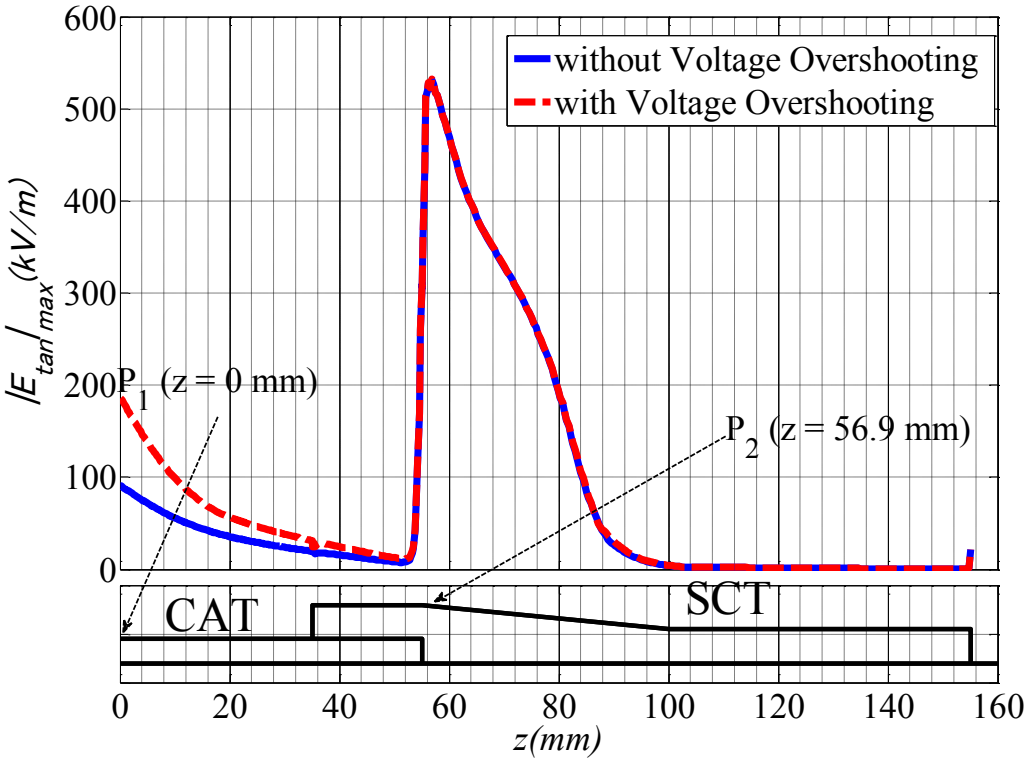

Fig. 3-17: *Comparison of maximum tangential electric field stress on the surfaces of the SGS under the 11L SCHB voltages between the two cases without and with voltage overshooting.*

Fig. 3-17 displays a comparison of maximum tangential electric field stress on the surfaces of the SGSs under the applied voltages of the 11L SCHB VSC between the two cases without and with voltage overshooting. It is demonstrated that the overshot voltage at the motor side has a significant impact on the electric field stress on the surfaces of the CAT while a very little effect of this factor can be recognized on the SCT. To give more detailed view about the above difference, the tangential electric field stress on the surfaces of the CAT at z = 0 mm and of the SCT at z = 56.9 mm during two intervals from 10.72 ms to 10.75 ms and from 12.445 ms to 12.475 ms are presented in Fig. 3-18 and Fig. 3-19, respectively. In the first interval, the duration of the impulse is too short for the overshot voltage to decay and hence, a high voltage rise of 4.113 kV/μs

occurs. Meanwhile, in the second interval, the overshot voltage is fully damped, and hence a lower voltage rise of 2.579 kV/μs appears. The higher voltage rise in the first interval causes higher electric field stress at z = 0 mm than the one in the second period. It is observed in the two above figures that the ringing voltages cause increases in both the intensity and the lasting time of tangential electric field stress on the CAT. On the other hand, at the position of z = 56.9 mm on the SCT, a little change of the tangential electric field by the overshot voltage is observed.

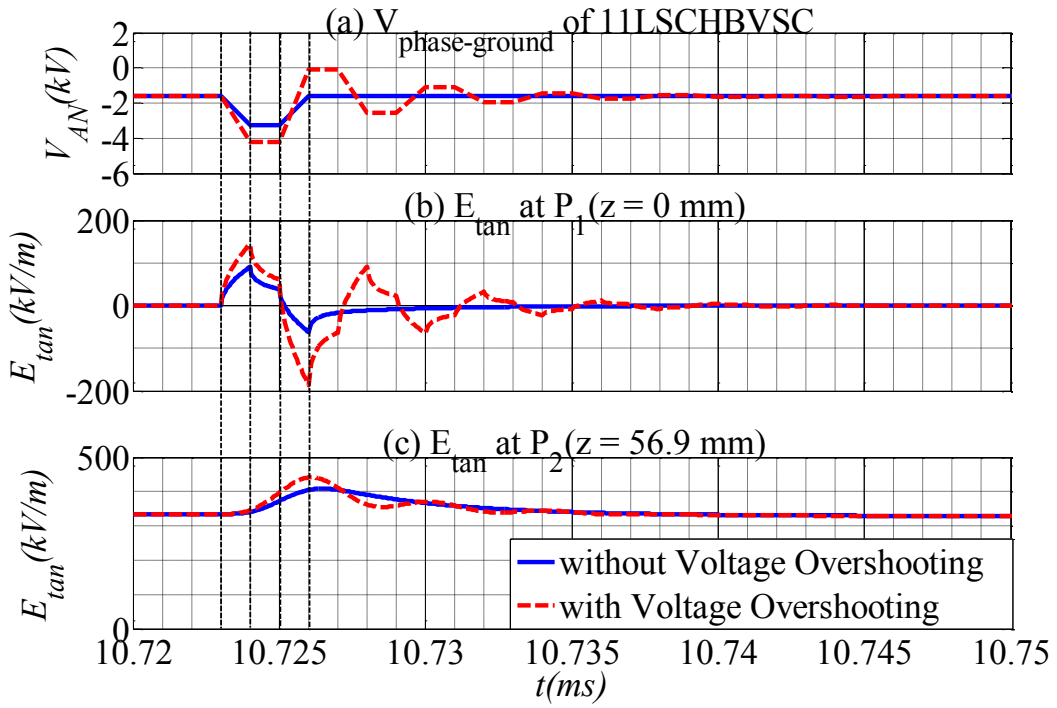

Fig. 3-18: *Tangential electric field on the surfaces of the SGS at the two points (z = 0 mm and z =56.9 mm) in the cases of 11L SCHB voltages during the interval from 10.72 ms to 10.75 ms.*

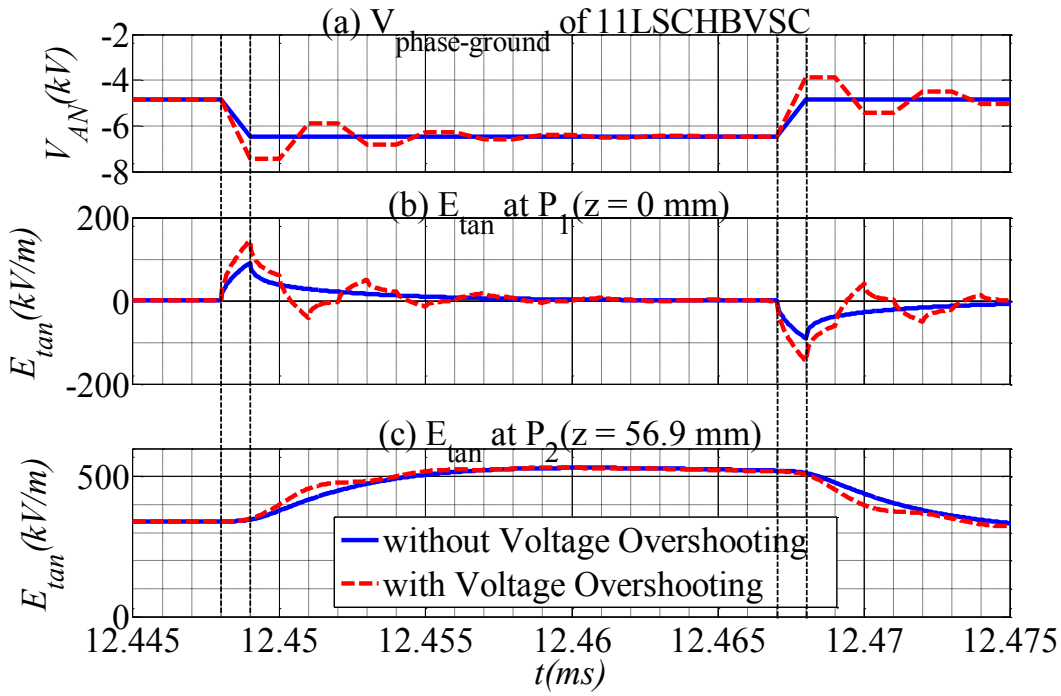

Fig. 3-19: *Tangential electric field on the surfaces of the SGS at the two points (z = 0 mm and z = 56.9 mm) in the cases of 11L SCHB voltages during the interval from 12.445 ms to 12.475 ms.*

Beside the tangential electric field stress, a significant increase of the dissipated power density inside the CAT caused by the overshot voltage, especially at the area near the stator slot exit, can be validated in Fig. 3-20. As a result, the increase of the heating process inside the SGS can be observed through the temperature distributions on the surfaces of this structure in the two cases in Fig. 3-21. From these results, it is demonstrated that the overshot effect in the PWM voltages can cause a high temperature rise in the SGS, especially at the region near the stator slot exit.

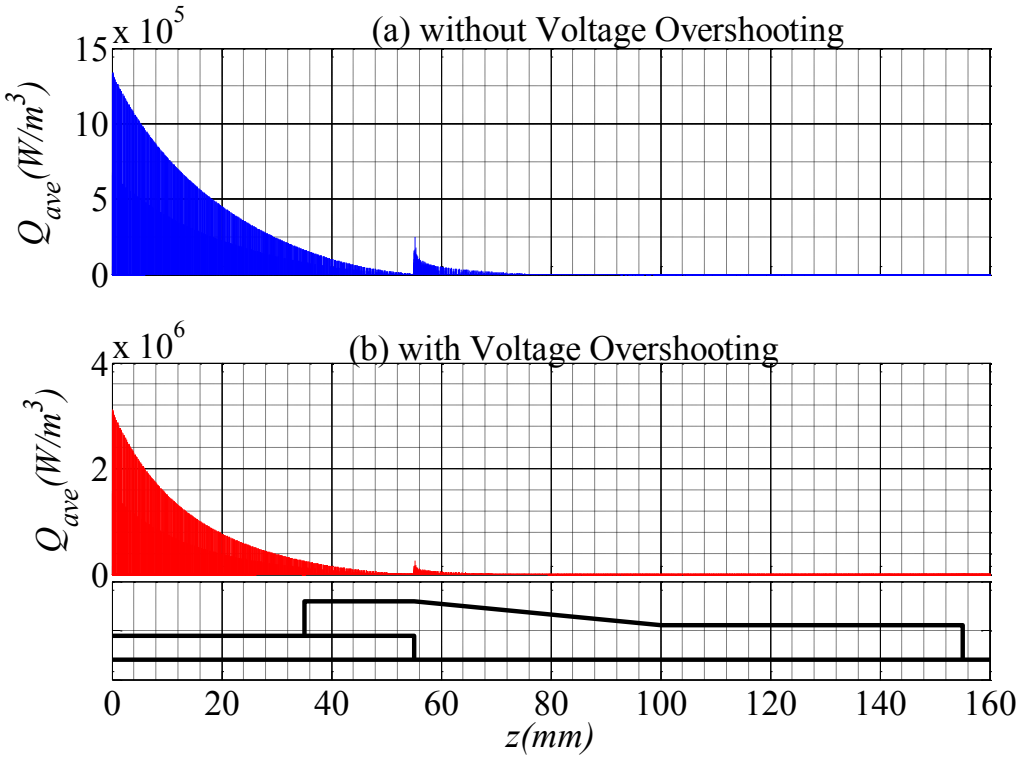

Fig. 3-20: *Maximum value along z-axis of average dissipated power density in the SGS in the cases of 11L SCHB voltages without and with voltage overshooting.*

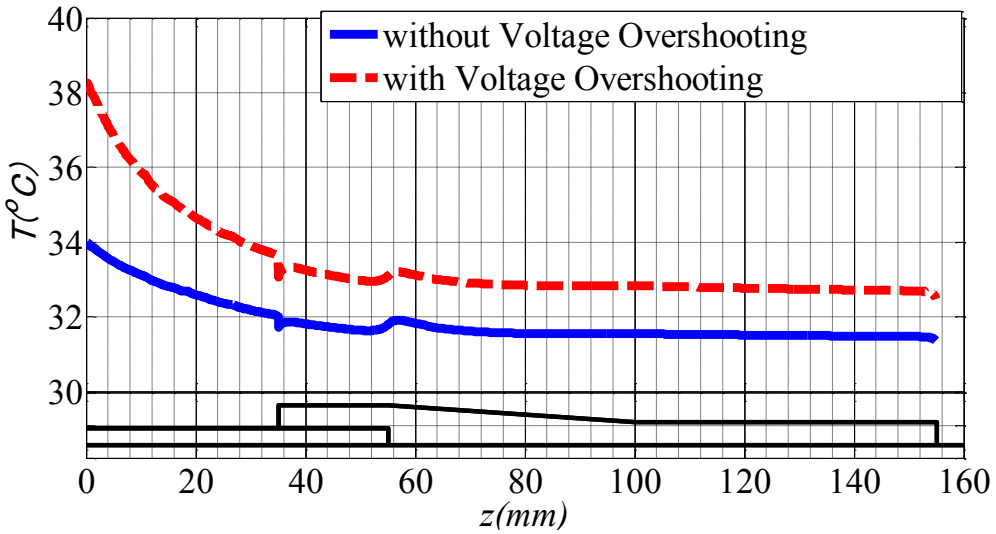

Fig. 3-21: *Temperature distribution on the surfaces of the SGS in the cases of 11L SCHB voltages without and with voltage overshooting after 30 hours.*

3.3.2 Typical cases

As already mentioned in the previous subsection, the overshot voltage has a very little effect on the electric field stress on the SCT. Hence, in these following cases, the main objective is to analyze the electric field stress on the CAT under the overshot voltages caused by different data of voltage rise time, cable length and motor impedance.

In commercial inverters, the range of voltage rise time t_r is from 50 ns to 2000 ns [2]. Hence, in these cases, the typical values of this parameter of 50 ns, 100 ns, 200 ns, 300 ns, 400 ns, 500 ns and 1000 ns are chosen for analyzing. Besides, surge impedance, a frequency dependent parameter, requires different and complicated techniques to measure [45, 47-48]. For this general computation, the surge characteristic of the inverter, the cable and the motor are the same as the ones in Table 3-5 in the previous subsection, except the impedance of motor which is selected between the two values of 100 Ω and 1000 Ω.

In the process of voltage reflection at motor terminal, a definition of cable critical length has to be reintroduced. This parameter is used to identify the length of cable where the overshoot in PWM voltage fully occurs and it can be calculated by equation (3-2) [49]. In this formula, t_r (s) and v (m/s) are the rise time of PWM voltage and travelling velocity of the surge through the cable, respectively. The resulted critical lengths corresponding to the rise time of 50 ns, 100 ns, 200 ns, 300 ns, 400 ns, 500 ns and 1000 ns are respectively 3.75 m, 7.5 m, 15 m, 22.5 m, 30 m , 37.5 m and 75 m.

$$l_c = \frac{vt_r}{2} \quad \text{(3-2)}$$

It is necessary to come back and look at the PWM voltage of the 11L SCHB VSC reaching the motor terminal in Fig. 3-19a. In this fundamental case, the overshot voltage is observed with 4 μs scaled oscillation with the equivalent frequency of 250 kHz. In cases of shorter voltage rise time (for example, 50 ns) or shorter length of cable, the oscillation can occur in the range much lower than 1 μs, the electric field analysis with the sampling increment of 0.05 μs cannot provide enough information for the SGS behavior. Hence, this analysis needs to be conducted with ns-sampling time. However, this restriction makes the electric field analysis of the SGS cost an enormous time for computation. Therefore, a simple waveform in Fig. 3-22 is used to replace the PWM voltage of the 11L SCHB VSC. It is noted that the duration of the impulses in this waveform is 30 μs, and this interval is long enough for the overshot voltage to decay before the next impulse.

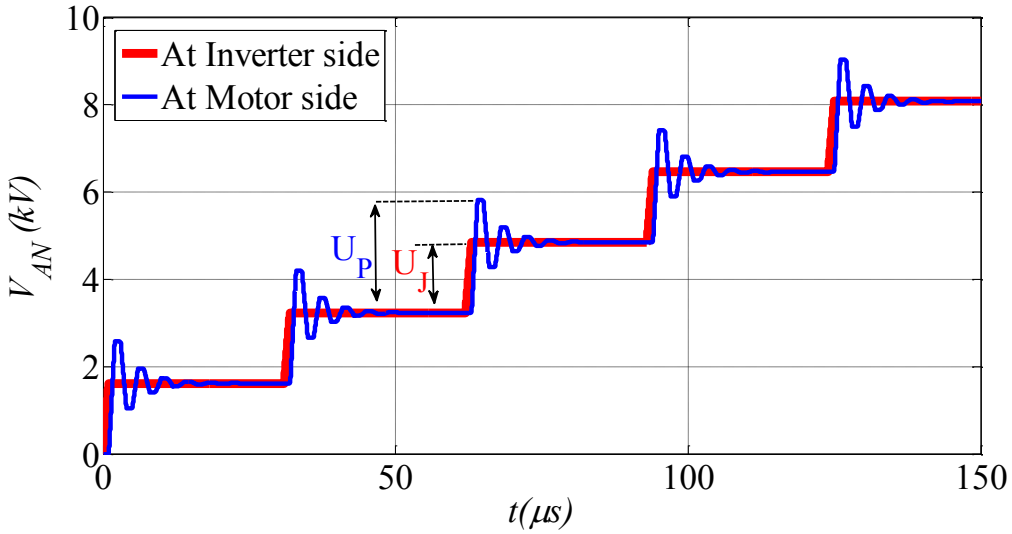

Fig. 3-22: *Simplified waveform of the 11L SCHB VSC used in the ns-scaled electric field analysis.*

A comparison of tangential electric field stress at the stator slot exit (z = 0 mm) on the surfaces of the CAT between this voltage and the 11L SCHB PWM one is presented in Fig. 3-23. In this example, the simplified voltage is used to analyze the electric field in the SGS using the same data of the fundamental case with the sampling time of 2.5 ns. It is observed that the substituting voltage causes the same electric field stress on the CAT as the PWM one. Hence, this simplification is a reasonable way to overcome the limitation of calculation time and it can provide an exact view about the impact of voltage overshooting phenomenon on the SGS, especially at the CAT area. Using this waveform, we can analyze the electric field in the SGS with the sampling increment of 2.5 ns.

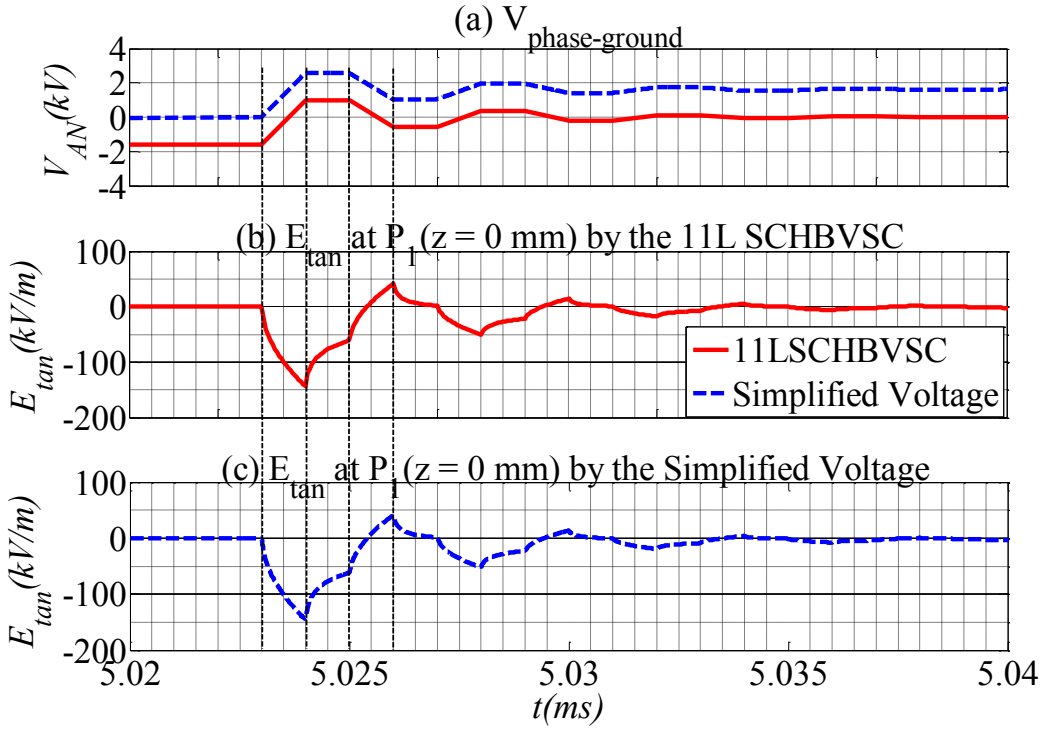

Fig. 3-23: *Tangential electric field stress at z = 0 mm on the surface of the CAT under the simplified and the 11L SCHB voltages.*

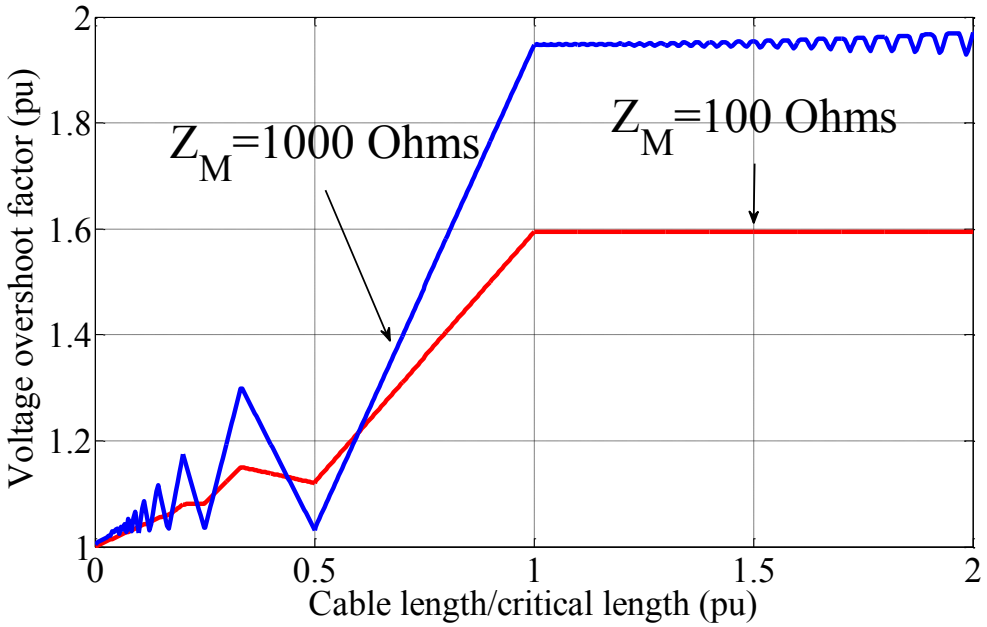

Fig. 3-24: *Voltage overshot factor versus the cable length for the two motor impedance values of 100 Ω and 1000 Ω.*

Fig. 3-24 presents the voltage overshoot factor U_P/U_J versus the length of cable for the two motor impedance values Z_M of 100 Ω and 1000 Ω. Note that, U_P and U_J are the peak and the jump voltages defined in Fig. 3-22. In some cases, cables are very long compared to the critical length, voltage overshoot factor can pass the threshold of 2 pu, and severe electric stresses occur on the insulation structure of motors. However, these rough cases are kept out of the theme of this investigation because three typical cable lengths, equivalent to 0.5, 1.0 and 1.5 critical value are chosen for each value of the voltage rise time to analyze the electric field stress on the SGS.

The characteristic curves of the maximum tangential electric field stress on the surface of the CAT at z = 0 mm versus the voltage rise time are presented in Fig. 3-25 to give a basic view about the impact of the overshot voltages in an interactive process among the inverter, the cable and the motor. The shorter the rise time is, the higher the rise rate of inverter voltage is, and the much higher the

stress that the CAT suffers from. Besides, the critical length of cable is a significant parameter to be noticed in the application of ASD systems.

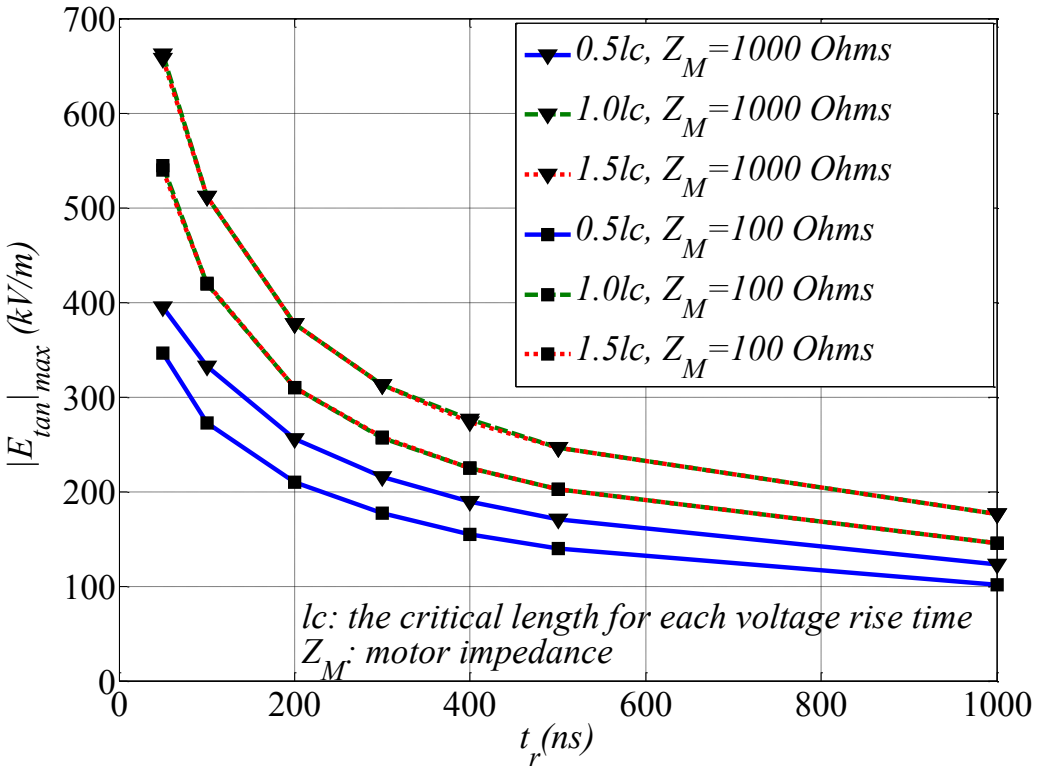

Fig. 3-25: *Maximum tangential electric field on the CAT at z =0 versus the rise time of the inverter voltages.*

Chapter 4

DISCUSSION

4.1 Electric field and thermal stresses in the SGS

It is observed from the frequency response of the SGS that the working ability of the SGS decreases with the increase of the applied frequency. This problem is due to the dielectric relaxation process of the materials in the SGS [28]. In the SGS, the CAT and the main insulation form a low pass filter displayed in Fig. 4-1 [50-51]. The cut-off frequency of this filter equivalent to the 55 mm long CAT which is calculated using (4-1) is 20.24 kHz. The output frequency response of this circuit is estimated using (4-2) and obtained in Fig. 4-2. It is noted that V_O is the voltage applied on the SCT and the main insulation while the one applied on the CAT, V_{CAT} can be determined in (4-3).

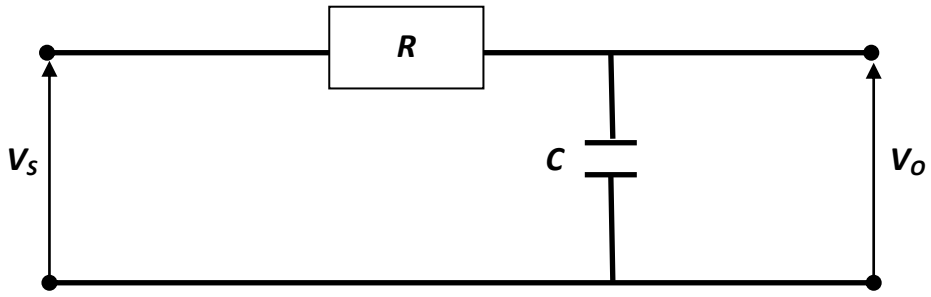

Fig. 4-1: RC *low pass filter circuit.*

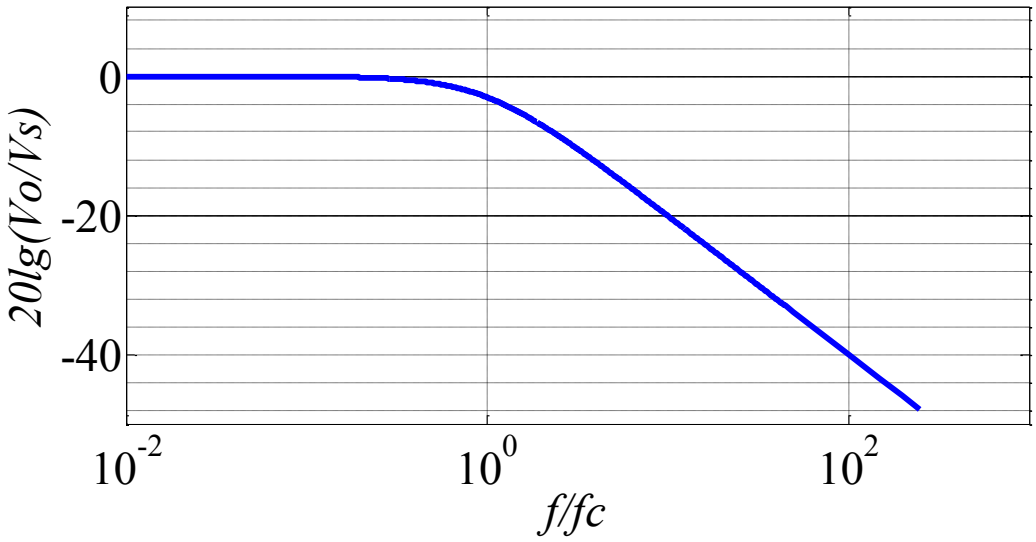

Fig. 4-2: *Frequency response of a low pass filter output.*

$$f_c = \frac{1}{2\pi RC} \quad \text{..... (4-1)}$$

$$V_O = \frac{V_S}{\sqrt{1+(f/f_c)^2}} \quad \text{..... (4-2)}$$

$$V_{CAT} = \sqrt{V_S^2 - V_O^2} \quad \text{..... (4-3)}$$

It is observed in Fig. 3-4 that on the segment of the SCT from z = 100 mm to z = 155 mm, the electric field is very small, hence, the electrical conductivity in this area can be considered as the one with zero field, 1.85 nS/m. The second low pass filter formed by this SCT segment and the main insulation has the cut-off frequency of 0.005 Hz. As a result, the output voltage from the first low pass filter of the CAT, V_O only applies on the SCT for the frequency from 50 Hz. The ratios of the voltage components applied on the CAT and the SCT to the phase to ground voltage applied between the conductor bar and the stator lamination are calculated using (4-2), (4-3) and displayed in Table 4-1 for the four cases of 50 Hz, 26 kHz, 123 kHz and 5 MHz. These results can be used to explain the decrease in the working ability of the SGS as observed in chapter 3.

Table 4-1: *Voltage ratios of the CAT and the SCT*

f	50 Hz	26 kHz	123 kHz	5 MHz
V_{CAT}/V_S	0	0.789	0.987	1.000
V_{SCT}/V_S	1.000	0.614	0.162	0

For a segment of SCT with the length of l, its resistance can be roughly estimated as follows

$$R_{SCT} = \frac{l}{\bar{\sigma}_{ec} S} \quad \text{..... (4-4)}$$

where $\bar{\sigma}_{ec}$ and S are the average electrical conductivity and the cross-section area of this SCT segment, respectively.

The capacitance of the main insulation between this SCT segment the conductor can be calculated using (4-5). In this equation, ε is the permittivity of the main insulation while r_c and t_{ins} are the radius of the conductor and the thickness of the main insulation, respectively.

$$C_{INS} = \frac{2\pi l \varepsilon}{\ln\left(\frac{r_c + t_{ins}}{r_c}\right)} \quad \text{..... (4-5)}$$

In case a sinusoidal voltage with amplitude V_O and frequency f applied between one end of this SCT segment and the conductor, the voltage difference applied on the whole length of this segment can be estimated using (4-6).

$$V_D = \frac{2\pi f R_{SCT} C_{INS}}{\sqrt{1 + \left(2\pi f R_{SCT} C_{INS}\right)^2}} V_O \quad \text{..... (4-6)}$$

From the equations (4-4), (4-5) and (4-6), the effective length of the SCT correspondent to a specific ratio V_D/V_O can be expressed as follows

$$l_{eff} = \frac{\sqrt{\bar{\sigma}_{ec} S \ln\left(\frac{r_c + t_{ins}}{r_c}\right)\frac{V_D}{V_O}}}{2\pi\sqrt{f\varepsilon\sqrt{1-\left(\frac{V_D}{V_O}\right)^2}}} \quad \text{(4-7)}$$

Based on the equation (4-7), the decrease of the effective length of the SCT with the rise of the frequency observed in the simulation results can be clearly clarified.

In the cases of PWM voltages provided by the SCHB VSCs, the fast impulses with a rise time t_r have an equivalent high frequency, $f_e = 1/\pi t_r$ [48]. For example, the equivalent frequency correspondent to the rise time t_r = 1 μs is 318.31 kHz, and is much higher than the cut-off frequency of the CAT low pass filter. Hence, in the similar mechanism to the high frequency sinusoidal voltages, the fast impulses with this rise time cause high electric field stress on the CAT, especially at the stator slot exit during its rising time. Therefore, dissipated power loss highly concentrates inside the region near this point during this short interval. Besides, the highest tangential electric field stress which is mainly initiated by the fundamental and high frequency voltage components less than 20.24 kHz is observed at the transition area on the SCT near the end of the CAT. Although the power loss at this overlapping region lasts for a much longer time, its density is much smaller than that one in the CAT. Therefore, the average density of this loss in the CAT is significantly higher than in the SCT. The same observation as in [24] is obtained that the voltage rise time has a high influence on the power loss in the CAT, but little one in the SCT.

In the thermal aspect, assessing the safety of an insulation system under working condition is based on its critical temperature. This parameter of each component in the SGS depends on the constructive materials and the fabrication technologies. For example, a standard process used in the production of SGSs is the vacuum pressure impregnation. For industrial applications, class F is adopted as a universal standard for insulation systems of rotating machines [52]. The critical temperature (T_{max}) and the maximum temperature rise limitation (ΔT_{max}) of this class are 155 ^{o}C and 105 ^{o}C, respectively. For the application of the two inverters, the maximum temperature rises from the background (30 ^{o}C) are respectively 10.42 ^{o}C and 4.02 ^{o}C for the 5L and the 11L SCHB VSCs, and observed in the CAT region at the stator slot exit. These values are much higher than the one of the sinusoidal voltage. Moreover, in practical working conditions of rotating machines, copper and iron losses have a majority role in heat generation. Therefore, in the case of full load and SCHB VSC, the superposition of these main losses, the SGS dissipated power loss and the PD loss have to be paid attention because the total temperature rise can pass over the limitation ΔT_{max} and the temperature soars over the threshold T_{max} inside the insulation structure of the motor, especially for the cases of low level inverters. The lifetime of the machine is significantly shortened and it would be eventually broken down. Besides, a suitable cooling system in the inverter-controlled rotating machines can become an effective solution to prevent these catastrophic situations.

Another problem is the voltage overshooting caused by the cable-motor impedance mismatch. This phenomenon is basically similar to an increase of the voltage rise rate *dV/dt* along with an attenuated high frequency oscillation. Hence, this phenomenon strongly increases the intensity of the electric stress on the CAT, especially at the area near the exit of the slot, and also the power loss in this CAT

region while it only has a little impact on the SCT. Besides, the ringing voltages can extend the living time of the stress on the CAT, and cause a significant addition to the power loss in this area. As a result, the temperature in the SGS, especially in the CAT, goes up. The computation results for the voltage overshooting show that the cooperation among users, manufacturers of inverters, cables and motors is very important to prevent unpredictable high overshot voltages that can cause high electric stress on the insulation of the motors in practical ASD applications.

4.2 Validation of the FEM based analysis models

To clarify the accuracy, the two FEM based models are applied to analyze the model bar-coil used for the experiments in [50]. In our analysis, the cylindrical geometry of the stator coil has to be used to replace the bar one with the same cross-section area of the conductor. All the lengths and thicknesses of the components in this insulation are the same as the real ones in the experiments. The air temperature is 28 ^{o}C, and the convective heat transfer coefficient is 5 W/(m^{2}K) correspondent to the natural convection. The fast impulse voltage with the time to peak of 250 ns, the time to half value of 7.6 μs, and the peak value of 17 kV used in [50] can be described as the double exponential function in (4-8).

$$V_S(t) = 17.490\left[\exp(-94{,}899t) - \exp(-21{,}826{,}671t)\right](\text{kV}) \quad \text{..... (4-8)}$$

In thermal analysis, the average power density is a very important profile which has a key role to decide the accuracy of the computation. Hence, this profile from our electric field analysis is extracted and compared with that one from a new method suggested by S. A. Boggs, A. Kumada, and T. Yoshimitsu in [53]. This method is based on the coupled electric and thermal analysis in

COMSOL using an assumption that is all the materials in the SGS have the same thermal properties, and the thermal conductivity is very low. In this case, the thermal diffusion is very small, and hence the dissipate power density can be extracted from the temperature rise ΔT in the SGS after a duration $\Delta\tau$ using (4-9)[53].

$$\overline{Q}_{res} = \frac{\rho C_p \Delta T}{\Delta \tau} \quad \text{..... (4-9)}$$

where ρ and C_p are the mass density and the heat capacity.

The maximum values along z-axis of the average power density in the SGS are displayed in Fig. 4-3. This result shows a very good agreement between our model and the one in [53]. A little difference can be seen in this comparison because of computation error.

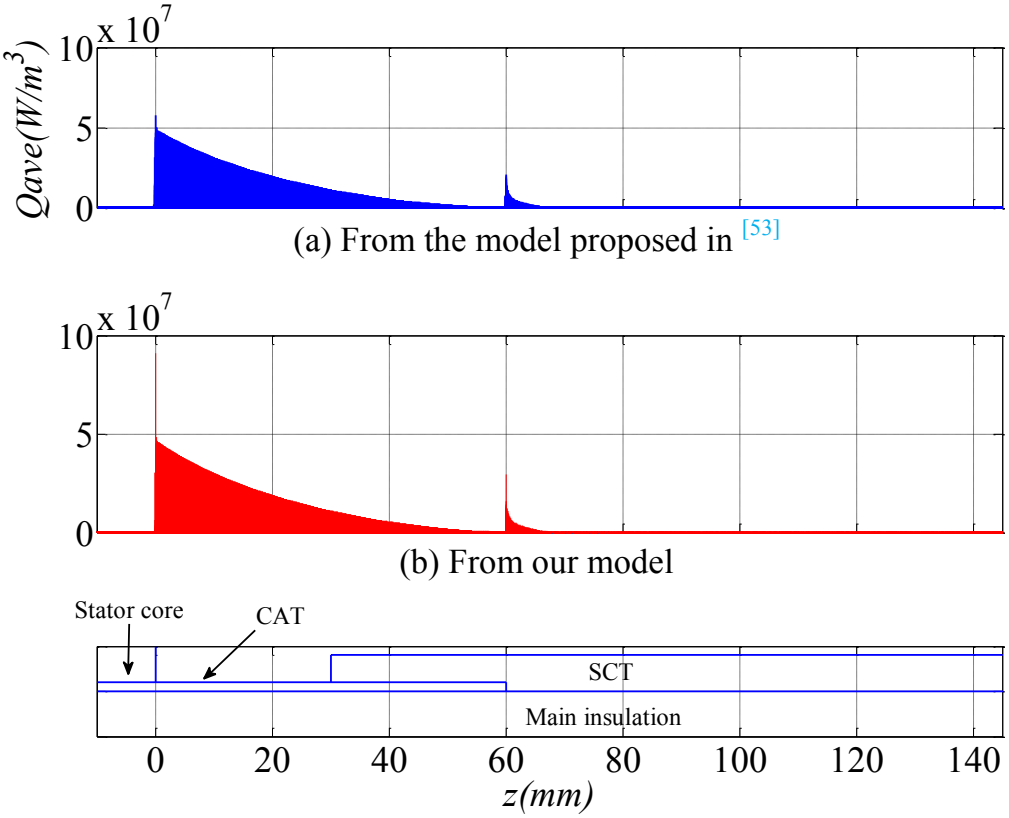

Fig. 4-3: *Maximum values along z-axis of dissipated power density in the SGS.*

The maximum tangential electric stress and the temperature on the surfaces of the SGS are illustrated in Fig. 4-4. From the electric field distribution, PD is supposed being initiated at the stator slot exit (z = 0 mm), at the starting point of the SCT (z = 30 mm) during the rise time of the impulse, and at the area on the SCT from the end of the CAT (z = 60 mm ÷ 71.6 mm) in the impulse tail. The highest surface temperature is observed on the CAT near the stator slot exit (z = 3.6 mm).

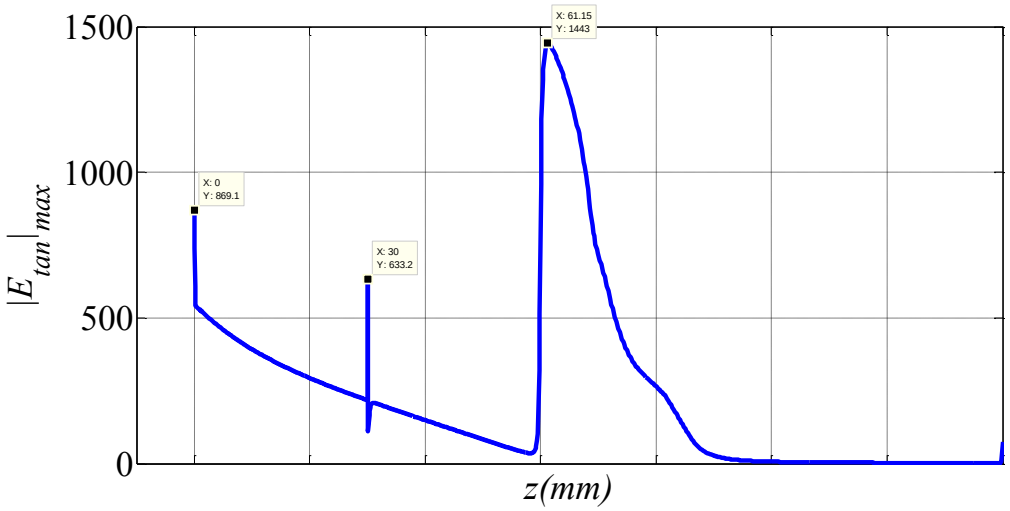

a) Maximum tangential electric stress on the surfaces of the SGS.

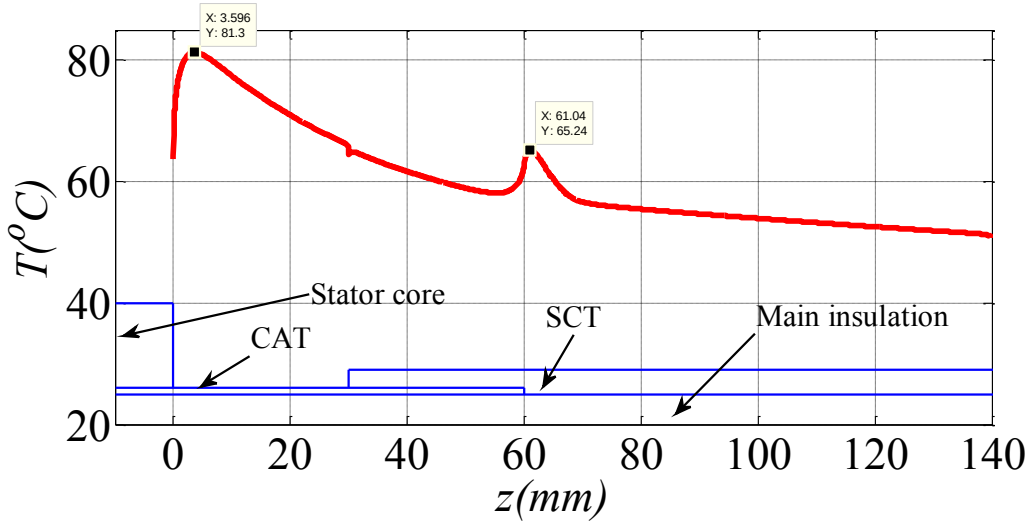

b) Temperature distribution on the surfaces of the SGS.

Fig. 4-4: *Computation results.*

Table 4-2: *Comparison between our computation and the experiment in* [50].

	Our computation	Experiment in [50]
Maximum temperature rise ΔT (°C)	53.3	60
Position of the hottest point z (mm)	3.6	14
Maximum electric stress $\|E_{tan}\|_{max}$ (kV/m)	1443	x
Position of maximum electric stress z (mm)	0 61.2	0 (before rise time) 66 (after rise time)

Table 4-2 summarizes the comparison between our computation and the experiment reported in [50]. There is a clear gap between the calculation and the experiment results. The first reason is the difference in the geometry of the SGS between our simulation and the experiment. The second one is that thermal energy generated by PD can locally increase the temperature at the high electric stress area in the measurement. Besides, another important factor is the electrical conductivity of the SCT. In our simulation, the DC electrical conductivity is used, and hence, it cannot exactly describe the nonlinear behaviour of the SGS under this fast impulse. In addition, the double exponential function of the impulse voltage in (4-8) is not exactly the same as the experimental one used in [50]. However, the computation results of the maximum temperature rise and of the position of highest electric stress are verified being consistent to the experimental ones. Moreover, our model can provide an estimation of tangential electric field on the surfaces of the SGS which is very difficult to achieve using measurement equipments. For example, a highly accurate Pockels sensor based

measurement apparatus used to measure the potential distribution on the surfaces of SGSs has a spatial resolution of 4 mm [50]. Hence, it cannot detect a highly local electric stress enhance on the surface area that is much smaller than its limited resolution. Fig. 4-5 is presented here to illustrate for this problem. In this case, a tiny triangular resin-filled crack appears in the middle of the CAT. It is noted that the electric conductivity of the resin is much lower than the CAT. Hence, in this example, this parameter of 10^{-6} S/m is chosen for the resin. From the computation result, the high electric field stress is observed and is supposed to initiate PD at the resin gap. This hypothesis of a high electrical resistant gap can be a good explanation for the PD recorded on the middle surface of the CAT in [29].

From the above validation, it is demonstrated that our analysis models can efficiently coordinate with laboratory tests to enhance the comprehensive of SGS behaviour in inverter voltage applied conditions.

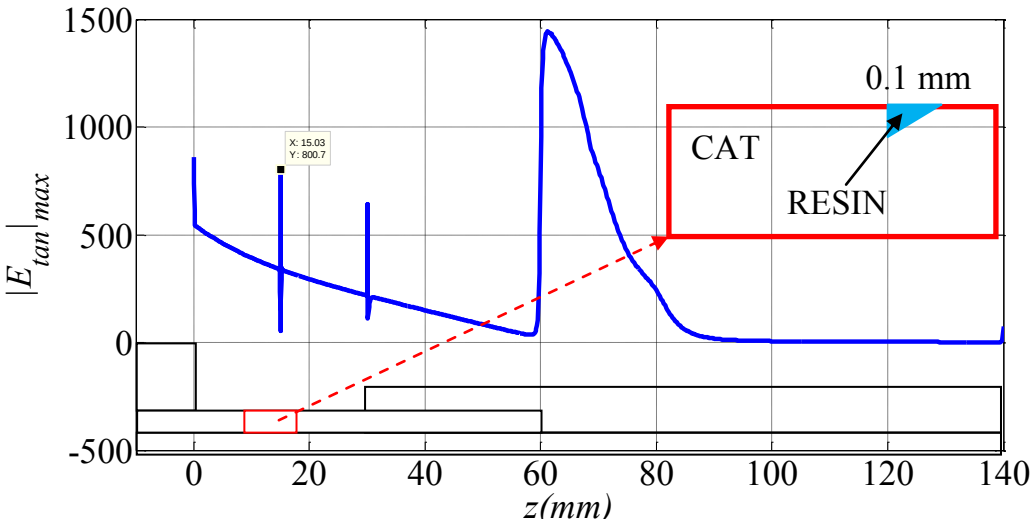

Fig. 4-5: *Hypothesis explained for PD on the middle surface of CAT in* [29].

Chapter 5
CONCLUSION AND FUTURE WORKS

5.1 Conclusion

Two analysis models of electric field and heat transfer are developed to give a comprehensive view of the electrical and the thermal stress grading mechanisms of the typical SGS under the PWM voltages of the SCHB VSCs. In the author's knowledge, this is the first time the thermal behaviour of a SGS is analyzed successfully in these fast impulse conditions. Besides, these models are supposed being able to use for all waveforms of the applied voltage.

The frequency response of the SGS can give a fundamental assessment of the working ability of this insulation structure in the high harmonic environments.

Although the high electric field stress is observed at the overlapping area between the CAT and the SCT, the dissipated power is confirmed to concentrate in the CAT region near the stator slot exit in the application of inverter-fed motors. In these PWM voltage applied conditions, high temperature rise caused by the dissipated power and PD in the SGS is an important factor that needs special attention, especially in design of cooling systems in the motors.

Voltage overshooting caused by impedance mismatch at the motor side has a significant impact on both the electrical and the thermal stresses in the CAT portion near the stator slot exit. This phenomenon increases not only the intensity but also the lasting time of these stresses. The SCT is demonstrated to become ineffective in preventing the harmful influence of this phenomenon, especially in the applications of long connecting cables, high ratios of motor surge impedance to cable one, and newer inverters with very fast electronic switches. Hence, to enhance the stress-levelling ability of this structure in the above conditions, the behaviour of CAT has to be improved. This information is supposed being a precious orientation for electric rotating machine manufacturers in the improvement designs of SGS in motors in ASD application. In order to prevent the unexpected voltage overshooting in this application, the cooperation among the users, the producers of motors, cables and inverters is very important indeed.

The application of these simulation models is an economic and efficient way together with laboratory tests for the operation analysis and the optimal design of SGSs.

5.2 Future Works

To increase the accurate level in the stress grading operation analysis of SGSs under fast impulse conditions, the equivalent electrical conductivity of the SCT has to be determined and used instead of the DC one. This is a very challenging issue needed many efforts with a very huge amount of experimental measurements.

The improvement design of SGSs for ASD applications is an inevitable requirement. In order to satisfy this demand, there are two typical directions

which focus on the fabrication of nonlinear materials used to produce SCTs and on the structural modification of SGSs. In the first direction, there have been many attempts to enhance the electrical and the thermal properties of available nonlinear materials such as Silicon Carbide and Zinc Oxide [9, 21] while many researchers have tried to explore new nonlinear materials [54] or PD highly resistant ones [6, 55]. In the latter, multilayered and sleeved structures of SGSs together with capacitive stress grading designs using potential floating foils inserted in the main insulation of SGSs were validated to be able to improve the stress relieving operation in fast impulse conditions of inverters [18-19, 22-23]. However, these structural modifications are still very complicated and somehow impossible in the practical manufacture of SGSs. Therefore, more breakthrough studies in both directions are still required. Besides, improvement studies of CAT using new materials or structural modifications are needed.

Together with the efforts to upgrade the working ability of SGSs, mitigation of the electrical and the thermal stresses caused by fast impulses of inverter sources can be a prospective solution. The use of sinusoidal filters for medium voltage ASD is very limited because these devices are complicated and expensive for low switching frequency in this application [26]. Hence, modified designs of these filters for medium voltage ASD applications can be a good answer for this problem. Besides, during the switching between stages of ASDs, unexpected voltage jumps can rarely occur as described in [2], and it is required that SGSs have to be designed to withstand these tough stresses. If these unexpected voltage leaps are absolutely prevented, economic and effective structures of SGSs can be achieved. Hence, the improvement in the control strategies of ASDs can be an attractive topic.

The measurement system based on Pockels sensor is demonstrated to be flexible and accurate for the electric potential distribution on the surfaces of SGSs in inverter source conditions. From the last discussion in Chapter 4, the space resolution of this system needs some improvements to assess the stress grading ability of SGSs.

Appendix A

LIST OF PUBLICATION

Journal papers

[1] **Nguyen Nhat Nam** and Satoshi Matsumoto, "Electrical and Thermal Computation of Stress Grading System in Inverter-Driven Medium Voltage Motors," *IEEJ Transactions on Fundamentals and Materials*, vol. 133, no. 11, pp. 591-597, 2013.

International conference papers

[1] **Nhat Nam Nguyen,** and Satoshi Matsumoto, "FDTD Method for the Electromagnetic Transient Behavior of Carbon Fiber Reinforced Plastic," *6th Asia Modeling Symposium*, pp. 231-235, May 2012.

[2] Ryuichi Ogura, Zulkarnain A. Noorden, **Nguyen Nhat Nam,** and Satoshi Matsumoto, "Comparison of Terahertz and Infrared Spectroscopy for Degraded Hydrocarbon Liquid," *Annual Report Conference on Electrical Insulation and Dielectric Phenomena*, pp. 455-458, October 2012.

[3] **Nguyen Nhat Nam,** and Satoshi Matsumoto, "Electric Field Calculation for Non-linear Stress-Grading Systems under Inverter-driven Rotating Machines," *7th South East Asian Technical University Consortium Symposium*, March 2013.

[4] **Nguyen Nhat Nam,** and Satoshi Matsumoto, "Operation Analysis of Stress Grading System in Inverter-Driven Medium Voltage Motors," *48th International Universities' Power Engineering Conference*, September 2013.

[5] **Nguyen Nhat Nam,** and Satoshi Matsumoto, "Effects of Conductive Armour Tape on the Behaviour of Stress Grading System in Inverter-driven Medium Voltage Motors," *8th South East Asian Technical University Consortium Symposium*, March 2014.

[6] **Nguyen Nhat Nam,** and Satoshi Matsumoto, "Operation Analysis of Stress Grading System in Medium Voltage Motors under a Typical Interactive Process among Inverter, Cable and Motor," *The International Conference on Electrical Engineering*, pp. 1313-1318, June 2014.

[7] Satoshi Matsumoto, **Nguyen Nhat Nam**, Daichi Nagaba, and Takahiro Ogiya, "PartialDischarge Characteristics of Twisted Magnet Wire under High Frequency AC Voltage," *The International Symposium on Electrical Insulating Materials*, pp. 57-60, June 2014.

Domestic conference and meeting papers

[1] **Nguyen Nhat Nam,** Vu Phan Tu and Satoshi Matsumoto, "Validating the Effect of Lightning Current Rise-Slope in Transient Response of Grounding Systems using Non-uniform Transmission Line Model," *Young Researcher Seminar of The Institute of Engineers on Electrical Discharges in Japan*, November 2011.

[2] **Nguyen Nhat Nam** and Satoshi Matsumoto, "FDTD Method for the Electromagnetic Transient Analysis of Carbon Fiber Reinforced Plastics," *Young Researcher Seminar of The Institute of Engineers on Electrical Discharges in Japan*, November 2012.

[3] **Nguyen Nhat Nam** and Satoshi Matsumoto, "Electric Field Analysis for Stress Grading System used in Inverter-Driven Medium Voltage Rotating Machines," *IEE Japan Technical Meeting on High Voltage Engineering*, pp. 13-18, January 2013.

[4] **Nguyen Nhat Nam** and Satoshi Matsumoto, "Electrical and Thermal Models of Stress Grading System in Inverter-Driven Medium Voltage Motors," *Young Researcher Seminar of The Institute of Engineers on Electrical Discharges in Japan*, November 2013.

REFERENCES

[1] Hiller M., Sommer R. and Beuermann M., "Medium-Voltage Drives," *IEEE Industry Applications Magazine*, vol.16, no.2, pp.22-30, 2010.

[2] IEC 60034-18-42, "Qualification and acceptance tests for type II electrical insulation systems used in rotating electrical machines fed from voltage converter", 2008.

[3] Roberts A., "Stress grading for high voltage motor and generator coils," *IEEE Electrical Insulation Magazine*, vol.11, no.4, pp.26-31, 1995.

[4] Espino-Cortes F.P., Cherney E.A. and Jayaram S., "Effectiveness of stress grading coatings on form wound stator coil groundwall insulation under fast rise time pulse voltages," *IEEE Trans. on Energy Conversion,* vol.20, no.4, pp.844-851, 2005.

[5] Brütsch R. and Chapman M., "Insulating systems for high voltage rotating machines and reliability considerations," *IEEE Int. Sym. on Electrical Insulation*, pp.1-5, 2010.

[6] Allison J.A., "Understanding the need for anti-corona materials in high voltage rotating machines," *Int. Conf. on Properties and Applications of Dielectric Materials,* vol.2, pp.860-863, 2000.

[7] Ul Haq S. and Omranipour R., "Comparative evaluation of various grading systems for electric machinery stator windings", *IEEE Int. Sym. on Electrical Insulation*, pp.1-4, 2010.

[8] Donzel L., Greuter F. and Christen T., "Nonlinear resistive electric field grading Part 2: Materials and applications", *IEEE Electrical Insulation Magazine*, vol.27, no.2, pp.18-29, 2011.

[9] C. Vanga-Bouanga, et al., "Tailoring of the Electrical Properties of Silicon Carbide for Field Grading Application," *IEEE Electrical Insulation Conf.* , pp.263-266, 2013.

[10] Gorur G. Raju, *Dielectric in Electric Fields,* Marcel Dekker Inc., pp. 97-100, 2003.

[11] Sharifi E., Jayaram S.H. and Cherney E.A.: "Temperature and electric field dependence of stress grading on form-wound motor coils," *IEEE Trans. on Dielectrics and Electrical Insulation*, vol.17, no.1, pp.264-270, 2010.

[12] Sharifi E., Jayaram S.H. and Cherney E. A., "AC modeling and anisotropic dielectric properties of stress grading of form-wound motor coils," *IEEE Trans. on Dielectrics and Electrical Insulation*, vol.17, no.3, pp.694-700, 2010.

[13] Jean P. Rivenc and Thierry Lebey, "An overview of electrical properties for stress grading optimization," *IEEE Trans. on Dielectrics and Electrical Insulation*, vol.6, no.3, pp.309-318, 1999.

[14] A. E. Baker; A. M. Gully and J. C. G. Wheeler, "Finite element modelling of nonlinear stress grading materials for machine end windings," *Int. Conf. on Power Electronics, Machines and Drives*, pp.265-268, 2002.

[15] Staubach C., Pohlmann F. and Jenau F.: "Comparison of transient time-domain and harmonic quasi-static solution of electrical and thermal coupled numerical stress grading calculations for large rotating machines," *IEEE Int. Symp. on Electrical Insulation*, pp.209-213, 2012.

[16] Staubach C., Wulff J. and Jenau, F.: "Particle swarm based simplex optimization implemented in a nonlinear, multiple-coupled finite-element-model for stress grading in generator end windings," *IEEE Conf. on Optimization of Electrical and Electronic Equipment*, pp. 482-488, 2012.

[17] Wheeler J. C G, "Effects of converter pulses on the electrical insulation in low and medium voltage motors," *IEEE Electrical Insulation Magazine,* vol.21, no.2, pp.22-29, 2005.

[18] Wheeler J. C. G., et al., "Novel stress grading systems for converter-fed motors," *IEEE Electrical Insulation Magazine*, vol.23, no.1, pp.29-35, 2007.

[19] Espino-Cortes F.P., Cherney E.A. and Jayaram S.H., "Impact of inverter drives employing fast-switching devices on form-wound AC machine stator coil stress grading," *IEEE Electrical Insulation Magazine*, vol.23, no.1, pp.16-28, 2007.

[20] Wheeler J. C G; et al., "Thermal performance of stress grading systems for converter-fed motors," *IEEE Electrical Insulation Magazine*, vol.23, no.2, pp.5-11, 2007.

[21] Chen W., Gao G. and Mouton C. A., "Stator insulation system evaluation and improvement for medium voltage adjustable speed drive applications," *55th IEEE Petroleum and Chemical Industry Technical Conf.,* pp.1-7, 2008.

[22] Sharifi E., Jayaram S. and Cherney E. A., "Capacitive Grading of 13.8 kV Form-Wound Motor Coil Ends for Pulse Width Modulated Drive Operation," *IEEE Int. Sym. on Electrical Insulation,* pp.632-635, 2008.

[23] Sharifi E., et al., "IEC qualification test applied to capacitively graded 13.8 kV bar samples energized with repetitive fast pulses," *Electrical Insulation Conf.*, pp.402-406, 2011.

[24] Sharifi E., Jayaram S.H. and Cherney E. A., "Analysis of thermal stresses in medium-voltage motor coils under repetitive fast pulse and high-frequency voltages," *IEEE Trans. on Dielectrics and Electrical Insulation*, vol.17, no.5, pp.1378-1384, 2010.

[25] Sharifi E., Jayaram S.H. and Cherney E. A., "A coupled electro-thermal study of the stress grading system of medium voltage motor coils when energized by repetitive fast pulses," *IEEE Int. Sym. on Electrical Insulation*, pp.1-4, 2010.

[26] Espino-cortes F.P., Gomez P. and Ramirez J. D. B., "Modeling of heat generated on stress grading coatings of motors fed by multilevel drives," *IEEE Trans on Dielectrics and Electrical Insulation*, vol.18, no.4, pp.1328-1333, 2011.

[27] Akiko Kumada, Satoshi Matsumoto, Daigo Yonesu and Katsuhiko Harada, "Inter-university research on the influence of high frequeny surges on insulation system in inverter fed motors," *Joint Technical Meeting on Electrical Discharges, Switching and Protecting Engineering and High Voltage Engineering*, pp.57-61, 2012.

[28] Kiuchi K., et al., "The potential distribution measurement on the stress grading system of high-voltage rotating machines by using pockels effect," *Conf. on Electrical Insulation and Dielectric Phenomena,* pp.199-200, 2012.

[29] Takahiro Nakamura, et al., "Partial discharges on stress-grading system in converter-fed motor coil," *Young Researcher Seminar of The Institute of Engineers on Electrical Discharges in Japan*, November 2013.

[30] El-Kishky H., El-Said A. and Brown F., "High Frequency Performance of Nonlinear Stress Grading Systems," *IEEE Int. Power Modulators & High Voltage Conf.,* pp.584-587, 2008.

[31] El-Kishky H., El-Said A. and Brown F., "Performance of Non-Linear Stress-Grading Systems at Non-Sinusoidal Voltages," *IEEE Int. Power Modulators & High Voltage Conf.,* pp.307-310, -2008.

[32] J.P Rivenc, A. Loubière and T. Lebey, "Conformal mapping comparison of resistive and capacitive grading materials," *Journal of Electrostatics*, vol. 43, Iss. 2, pp.127-143, 1998.

[33] Egiziano L. et al., "A Galerkin model to study the field distribution in electrical components employing nonlinear stress grading materials," *IEEE Trans. on Dielectrics and Electrical Insulation*, vol.6, no.6, pp.765-773, 1999.

[34] Li W.A, et al., "Study on general governing equations of computational heat transfer and fluid flow," *Communications in Computational Physics*, vol.12, no.5, pp.1482-1494, 2012.

[35] Gunther Lehner, *Electromagnetic Field Theory for Engineers and Physicists*, Springer, pp. 108-110, 2010.

[36] Karl E. Lonngren and Sava V. Savov, *Fundamentals of Electromagnetics with Matlab*, Scitech Publishing Inc., pp. 385-391, 2005.

[37] Bertin Y., et al., "Thermal behavior of an electrical motor through a reduced model," *IEEE Transactions on Energy Conversion*, vol.15, no.2, pp.129-134, Jun 2000.

[38] Martin Hettegger, et al., "Identifying the heat transfer coefficients on the end-windings of an electrical machine by measurements and simulations," *XIX International Conference on Electrical Machines*, pp.1-5, 2010.

[39] http://www.engineeringtoolbox.com/emissivity-coefficients-d_447.html (03/02/2014).

[40] Abu-Rub H., et al., "Medium-Voltage Multilevel Converters—State of the Art, Challenges, and Requirements in Industrial Applications," *IEEE Trans. on Industrial Electronics*, vol.57, no.8, pp.2581-2596, 2010.

[41] Islam M.R., Youguang Guo and Jian Guo Zhu, "Performance and cost comparison of NPC, FC and SCHB multilevel converter topologies for high-voltage applications," *Int. Conf. on Electrical Machines and Systems*, pp.1-6, 2011.

[42] Endrejat F. and Pillay P., "Resonance Overvoltages in Medium-Voltage Multilevel Drive Systems," *IEEE Trans. on Industry Applications*, vol.45, no.4, pp.1199-1209, 2009.

[43] Kim Jae-Chul , Song Seung-Yeop and Lee Do-Hoon, “Analysis on the Switching Surge Characteristics of a High-Voltage Induction Motor Fed by PWM Inverter Using EMTP,” *KIEE Int. Trans. on Power Engineering*, vol.5-A, no.1, pp.22-30, 2005.

[44] Shendge A. and Nagaoka N., "A modeling method and EMTP simulations of an inverter surge," *Asia-Pacific Symp. on Electromagnetic Compatibility*, pp.109-112, 2012.

[45] Amarir S. and Al-Haddad K., "A Modeling Technique to Analyze the Impact of Inverter Supply Voltage and Cable Length on Industrial Motor-Drives," *IEEE Trans. on Power Electronics* , vol.23, no.2, pp.753-762, 2008.

[46] Schmerling R., et al., "Parameter studies on surface partial discharge inception of polluted, tangential electrically stressed boundary surfaces," *Electrical Insulation Conf.*, pp.115-119, 2011.

[47] Villefrance R., Holboll J.T. and Henriksen M., "Estimation of medium voltage cable parameters for PD-detection," *IEEE Int. Sym. on Electrical Insulation*, vol.1, pp.109-112 vol.1, 1998.

[48] Skibinski G., et al., "Reflected wave modeling techniques for PWM AC motor drives," *Applied Power Electronic and Exposition Conf.*, vol.2, pp.1021-1029, 1998.

[49] M. D. Texiera and J. A. Houdek, “Protecting Submersible Motors from the Effects of PWM Voltage,” *Brazil Conf. for Quality of Electric Energy,* 2009.

[50] A. Kumada, et al., “Transient Potential Distribution on Stress Grading System on Rotating Machines under Repetitive Impulse Voltages,” *Electrical Insulation Conf.,* June 2014.

[51] T. Nakamura, et al., “Potential Distribution on Stress Grading of Inverter-fed Rotating Machines under DC Biased Voltage,” *Int. Conf. on Electrical Engineering,* pp. 1289-1294, June 2014.

[52] Brandes H., et al., "Class H insulation system for rotating equipment", *IEEE Int. Sym. on Electrical Insulation*, pp.346-349, 2006.

[53] S. A. Boggs, A. Kumada, and T. Yoshimitsu, “Measurement of stress grading conductivity to 1.6 MV/m and 155 ^{o}C – Computation on grading power density and temperature rise for PWM waveforms,” *Int. Sym. on Insulating Materials ,* pp.54-56, June 2014.

[54] Schmerling R. et al., "Investigations of modified nonlinear electrical materials for end corona protection in large rotating machines," *47th International Universities Power Engineering Conf* ., pp.1-5, 2012.

[55] Yang Cao, Irwin P.C. and Younsi K., "The future of nanodielectrics in the electrical power industry," *IEEE Trans. on Dielectrics and Electrical Insulation*, vol.11, no.5, pp.797-807, 2004.